

Response to Referee #1 Comments

Point 1: Statement of the third key point is not very clear. After reading the manuscript, I know the main point is the west coastal area, but the statement is not emphasizing this.

Response 1: Agreed and the following text has been added in the Section 4.4:

“The highest rainfall erosivity regions in the UK are concentrated in the mountainous areas along the western coast, related to their rainfall system. The moist air brought by the prevailing westerly wind from the Atlantic Ocean moves from west to east across the UK and rises when it encounters the mountains of western England. Therefore, the mountainous regions along the UK western coast have the highest rainfall amount and rainfall erosivity in the UK. In addition, western Scotland is under the subpolar oceanic climate, which enhances its humidity. On the contrary, eastern Scotland and northeastern England are more likely to expose continental polar air mass, which brings dry and cold air and lower rainfall erosivity.”

Point 2: For interpolation of rainfall in section 4.1, CEH also published 1km gridded rainfall datasets for the whole UK, have you compared your interpolation rainfall with theirs? The reason I’m asking it is because rainfall interpolation is important in the following analysis of erosion, it’s worthy to ensure that the interpolation is reliable.

Response 2: CEH is a dataset with 1 km gridded estimates of daily and monthly rainfall for the whole UK derived from the Met Office. The natural neighbour interpolation methodology, including a normalisation step based on average annual rainfall, was used to generate the product (Tanguy et al., 2019). The method for calculating EI_{30} requires hyetograph data for individual storms (Wischemier and Smith, 1978). Therefore, the monthly or daily rainfall data generated by CEH are hard to distinguish rainfall events and estimate EI_{30} , although some studies have proposed methods related daily rainfall data to estimate rainfall erosivity using statistical models.

The study area has the little climatic variability with same climate type named temperate oceanic climate, and the 304 hourly rain gauges are distributed throughout the UK evenly. Therefore, ordinary kriging interpolation was expected to produce realistic results. It should be noted that refined interpolation for rain gauges is not the focus of this research. Instead, we tried to propose a methodology based on the numerical weather prediction model for estimating rainfall erosivity anywhere around the world, especially those regions with sparse instruments.

Tanguy, M.; Dixon, H.; Prosdocimi, I.; Morris, D.G.; Keller, V.D.J. (2019). Gridded estimates of daily and

monthly areal rainfall for the United Kingdom (1890-2017) [CEH-GEAR]. NERC Environmental Information Data Centre. (Dataset). <https://doi.org/10.5285/ee9ab43d-a4fe-4e73-afd5-cd4fc4c82556>.

Wischmeier, W. H. and Smith, D. D. (1978). Predicting rainfall erosion losses-a guide to conservation planning. Department of Agriculture, Science and Education Administration, US.

Point 3: The empirical equation in table 1 and figure 1 did not perform very well with R2 not over 0.50, how well is the relationship in other studies? Is this acceptable based on previous studies?

Response 3: The Figure 2 in the manuscript has been replaced with the following figures, which is clearer in showing the method performance. Van Dijk et al. (2002) compared the three forms of $ke-I$ relationships including exponential, logarithmic and power-law equations, based on the same observed data. The R^2 values are 0.53, 0.52 and 0.53, respectively. The R^2 values in this study is surely acceptable that many studies have obtained R2 value between 0.45-0.50 (Laws and Parsons, 1943; Kinnel, 1980; Brandt, 1988). Angulo-Martínez et al. (2016) compared simulated ke from 14 different exponential $ke-I$ relationships with respect to the disdrometer-observed values, found that R^2 was low at 1 min resolution (~ 0.25). The low R^2 of empirical equations also indicate the large variability of DSD in nature. Therefore, we believed that the study of large-scale rainfall energy and rainfall erosivity based on NWP-derived DSD is of great significance.

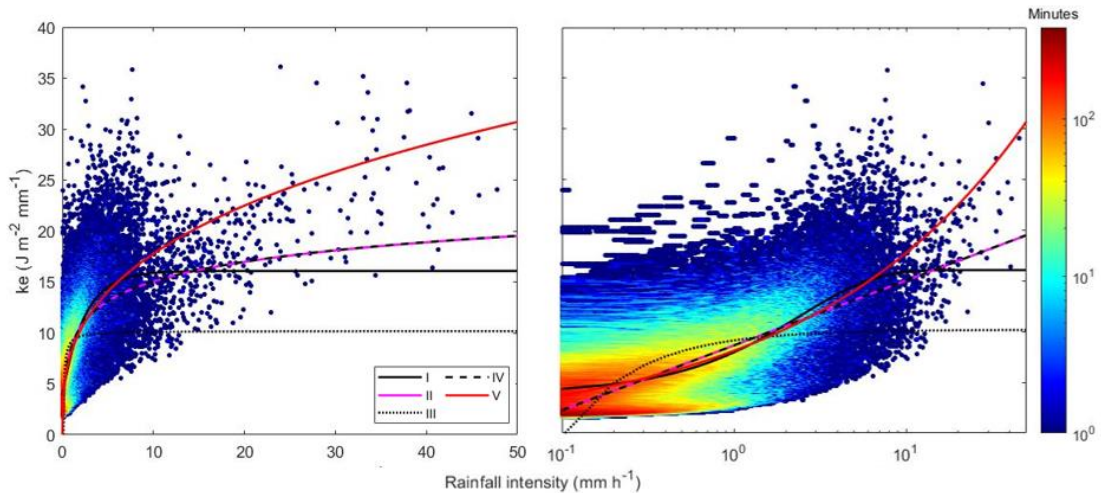


Figure 1 (new Figure 2 in manuscript). Minutes number per intensity class (x-axis) and ke class (y-axis) with five fitted $ke-I$ curves at Chilbolton station (2004–2013), plotted on linear (left) and logarithmic (right) intensity scales.

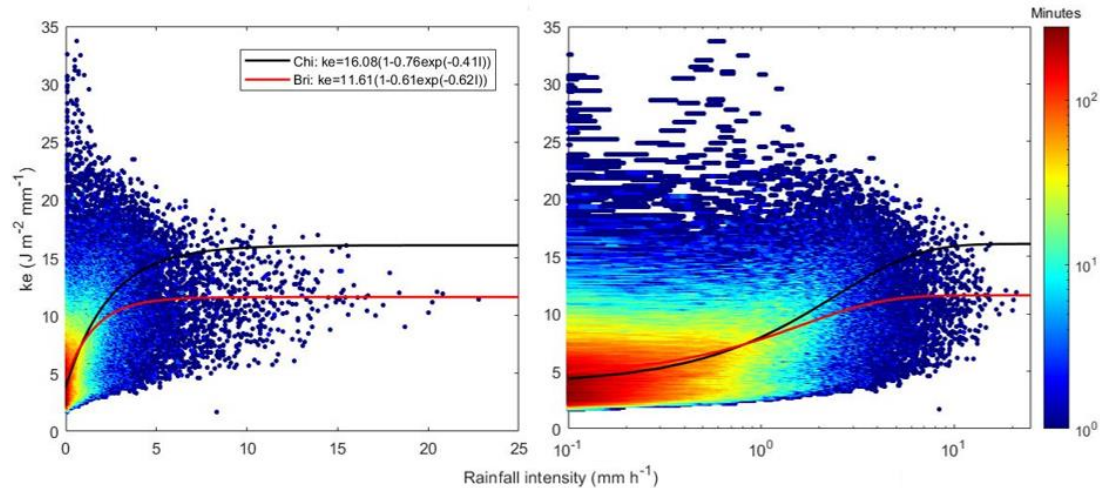


Figure 2 (new Figure 4 in manuscript). Minutes number per intensity class (x-axis) and ke class (y-axis) with fitted $ke-I$ curves at Bristol station (2015–2018), plotted on linear (left) and logarithmic (right) intensity scales.

Angulo-Martínez, M., Beguería, S. and Kysely, J. (2016). Use of disdrometer data to evaluate the relationship of rainfall kinetic energy and intensity (KE-I). *Science of the Total Environment* 568: 83-94.

Van Dijk, A., Bruijnzeel, L. and Rosewell, C. (2002). Rainfall intensity–kinetic energy relationships: a critical literature appraisal. *Journal of Hydrology* 261(1-4): 1-23.

Point 4: The two disdrometers are located in the same region, but the relationship is significantly different. Is it common in previous studies or any explanation about it?

Response 4: The current studies have showed that DSD and $ke-I$ relationships changes significantly with geographical locations and weather systems, including climate, altitude and terrain (Van Dijk et al., 2002; Angulo-Martínez et al., 2016). Both disdrometers located in southern England, have the similar oceanic climate. However, there are still differences between the two stations in altitude, topography, land cover, etc. For instance, Chilbolton Observatory is located on the edge of the village of Chilbolton, at an attitude of 86m, while University of Bristol is an urban campus, at 77m attitude. The former is 11 kilometers from the coastline and the latter is above 37 kilometers. From the revised Figure 2 and Figure 4, the difference in the $ke-I$ relationship between the two stations can be clearly observed. Moreover, the significant difference also shows that DSD-based estimation methods are needed to reflect rainfall microphysical characteristics on large-scale, which is the goal of this work.

Van Dijk, A., Bruijnzeel, L. and Rosewell, C. (2002). Rainfall intensity–kinetic energy relationships: a critical literature appraisal. *Journal of Hydrology* 261(1-4): 1-23.

Point 5: In figure 7, can you change the x axis tick to the real month, e.g. Jan/2013, so that seasonable patterns can be observed and analyzed?

Response 5: Agreed and amended. Figure 7 in manuscript has been changed and the following text has been added in the Section 4.3. We also added a figure (Figure 8) to show how monthly patterns performed.

“Based on the four-year data, the study area is rainy throughout the year with little R monthly, or seasonal patterns change (Figure 8), influenced by the temperate oceanic climate. Figure 8 also indicated that through the perspective of monthly average results, R_{W-WDM6} values are low, R_{W-TAA} has a good similarity with low R_D , and $R_{W-Morrison}$ is the closest to R_D in value.”

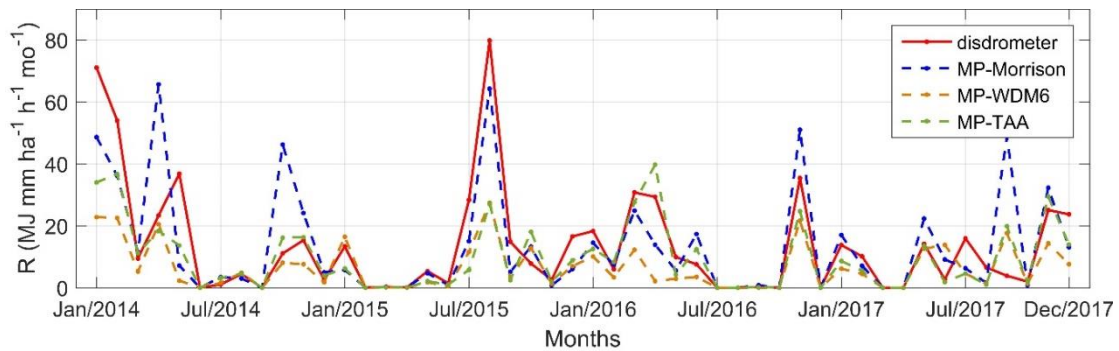


Figure 3 (new Figure 7 in manuscript). Comparison of disdrometer- and WRF-derived monthly rainfall erosivity estimations at Chilbolton station (2014–2017).

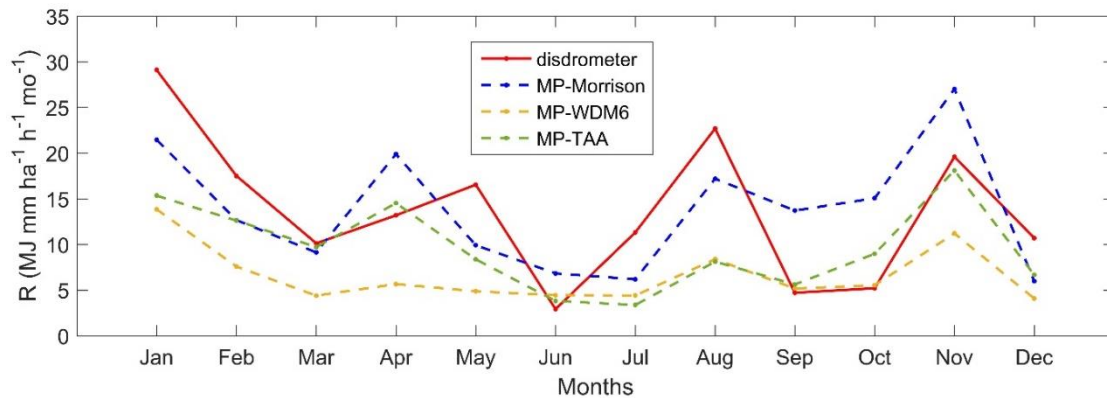


Figure 4 (added as Figure 8 in manuscript). Comparison of disdrometer- and WRF-derived average monthly rainfall erosivity estimations at Chilbolton station (2014–2017).

Point 6: Discussion part is weak in the manuscript, more discussions can be added in the result section or a separate section by comparing with previous studies and discussing about the potential limitations and applications of this approach.

Response 6: Discussion part is mainly contained in the conclusion section. The following text has been added in the Section 5 to enrich the discussion:

“The reliability of the WRF model is heavily dependent on the model-driving initial data provided by mesoscale or global models and complicated scheme setting and parameter adjustment (Liu et al., 2013; Thompson and Eidhammer, 2014; Kumar et al., 2017). However, numerous uncertainties are observed in the parameterization of the WRF simulation, and the choice of microphysical schemes has a significant influence on the inverted DSD (Ćurić et al., 2009; Yang et al., 2019). Therefore, combining the DSDs obtained by an increasing number of disdrometers and the WRF model is valuable. For example, the Disdrometer Verification Network (DiVeN) in the UK (Pickering et al., 2019) started in Feb 2017 can be introduced to support and improve our estimation in future studies.”

“Soil erosion in the UK is dominated by water erosion ($10\text{--}30\text{ t km}^{-2}\text{ yr}^{-1}$), especially in areas with abundant rainfall in Scotland, where the soil loss rate is approximately 5–10 times that of dry areas (Duck, 1996). Thus, it is significant to estimate rainfall erosivity to elucidate the microphysical characteristics of rainfall and rainfall–soil interactions. Benaud et al. (2020) collated empirical soil erosion observations from UK-based studies into a geodatabase. However, there is a limitation that this database does not cover the entirety of the UK, especially the limited records in northern Scotland. In our future work, we propose to compare the soil loss database with our estimated soil loss using WRF DSD based rainfall erosivity and a soil erosion model (such as RUSLE). We believe that not only can we better analyze the impact of rainfall and rainfall erosivity on the UK soil loss, but also help to better understand microphysical rainfall–soil interactions to support the rational formulation of soil and water conservation planning.”

Benaud, P., Anderson, K., Evans, M., Farrow, L., Glendell, M., James, M. R., ... & Brazier, R. E. (2020). National-scale geodata describe widespread accelerated soil erosion. *Geoderma*, 371: 114378.

Ćurić, M., Janc, D., Vučković, V. and Kovačević, N. (2009). The impact of the choice of the entire drop size distribution function on Cumulonimbus characteristics. *Meteorologische Zeitschrift* 18(2): 207-222.

Duck, R. W. (1996). Regional variations of fluvial sediment yield in eastern Scotland. *Erosion and Sediment Yield: Global and Regional Perspectives: Proceedings of an International Symposium Held at Exeter, UK, IAHS*.

Kumar, P., Kishtawal, C. and Pal, P. (2017). Impact of ECMWF, NCEP, and NCMRWF global model analysis on the WRF model forecast over Indian Region. *Theoretical and Applied Climatology* 127(1-2): 143-151.

Liu, J., Bray, M. and Han, D. (2013). Exploring the effect of data assimilation by WRF - 3DVar for numerical rainfall prediction with different types of storm events. *Hydrological Processes* 27(25): 3627-3640.

Pickering, B. S., Neely III, R. R., & Harrison, D. (2019). The Disdrometer Verification Network (DiVeN): a UK network of laser precipitation instruments. *Atmospheric Measurement Techniques* 12: 5845-5861.

Thompson, G. and Eidhammer, T. (2014). A study of aerosol impacts on clouds and precipitation development in a large winter cyclone. *Journal of the Atmospheric Sciences* 71(10): 3636-3658.

Yang, Q., Dai, Q., Han, D., Chen, Y. and Zhang, S. (2019). Sensitivity analysis of raindrop size distribution parameterizations in WRF rainfall simulation. *Atmospheric Research* 228: 1-13.

Response to Referee #2 Comments

Point 1: You have used two disdrometers in the same locations (considering the whole UK study area) and in the same elevation ranges (low elevation), but they differ considerably. What about the high elevation then? And how much they are representative of the whole UK?

Response 1: The current studies showed that DSD and *ke-I* relationships changes with geographical locations and weather systems, including climate, altitude and terrain (Van Dijk et al., 2002; Angulo-Martínez et al., 2016). Both the two disdrometers located in southern England, have the similar oceanic climate. The focus of this study is not to use disdrometers to estimate rainfall erosivity. On the contrary, we chose the two disdrometers in similar locations to illustrate the spatial uncertainty of the *ke-I* relationship exactly. The results indicated that it is inappropriate to rely on an empirical formula in a large scale. The widely used (R)USLE approach to predict *ke-I* relationships based on measurement at a single location only (Wischmeier et al., 1978; Renard et al., 1997). Therefore, the proposed method based on NWP DSD is expected to effectively improve large-scale rainfall KE and rainfall erosivity estimation.

Angulo-Martínez, M. and Barros, A. (2015). Measurement uncertainty in rainfall kinetic energy and intensity relationships for soil erosion studies: An evaluation using PARSIVEL disdrometers in the Southern Appalachian Mountains. *Geomorphology* 228: 28-40.

Renard, K. G., Foster, G. R., Weesies, G., McCool, D. and Yoder, D. (1997). Predicting soil erosion by water: a guide to conservation planning with the Revised Universal Soil Loss Equation (RUSLE), United States Department of Agriculture Washington, DC.

Van Dijk, A., Bruijnzeel, L. and Rosewell, C. (2002). Rainfall intensity–kinetic energy relationships: a critical literature appraisal. *Journal of Hydrology* 261(1-4): 1-23.

Wischmeier, W. H. and Smith, D. D. (1978). Predicting rainfall erosion losses-a guide to conservation planning. Department of Agriculture, Science and Education Administration, US.

Point 2: Could you use the recently published and open access Disdrometer Verification Network of UK (Disdrometer Verification Network (DiVeN): a UK network of laser precipitation instruments, <https://amt.copernicus.org/articles/12/5845/2019/>) to support the finding of your study and refine better the findings?

Response 2: This study used two disdrometers in Chilbolton and Bristol to calibrate *R* results derived by WRF

model. Both two disdrometers have long running periods and have been fully studied and calibrated from a series of research work by our team (Islam et al., 2012; Dai et al., 2014; Yang et al., 2019). The DiVeN disdrometer network may provide an interesting support for our follow-up research, such as finding an empirical formula that is most suitable for the UK as a whole. However, for this study, DiVeX has less overlap with the period studied here, which has limitations for verifying. The following text has been added at the end of Section 5:

“For example, the Disdrometer Verification Network (DiVeN) in the UK (Pickering et al., 2019) started in Feb 2017 can be introduced to support and improve our estimation in future studies.”

Dai, Q. and Han, D. (2014). Exploration of discrepancy between radar and gauge rainfall estimates driven by wind fields. *Water Resources Research* 50(11): 8571-8588.

Islam, T., Rico-Ramirez, M. A., Thurai, M. and Han, D. (2012). Characteristics of raindrop spectra as normalized gamma distribution from a Joss–Waldvogel disdrometer. *Atmospheric Research* 108: 57-73.

Pickering, B. S., Neely III, R. R., & Harrison, D. (2019). The Disdrometer Verification Network (DiVeN): a UK network of laser precipitation instruments. *Atmospheric Measurement Techniques* 12: 5845-5861.

Yang, Q., Dai, Q., Han, D., Chen, Y., and Zhang, S. (2019). Sensitivity analysis of raindrop size distribution parameterizations in weather research and forecasting rainfall simulation. *Atmospheric Research* 228:1-13

Point 3: The performance (R^2) of equations of the relationship between Ke -I presented in Table 1 are low and very similar (except ID-III). The exponential (ID-I) and power-law (ID-V) are exactly the same, and did not support the statement given in Line 73 where the exponential relationship is used in preference. Would you discuss this in detailed and how much these values are in line with former investigations?

Response 3: The figures below replaced Figure 2 in the manuscript, expressed the number of minutes per intensity class (x-axis) and ke class (y-axis). It clearly showed how the five equations performed, plotted on linear and logarithmic intensity scales, respectively. Figure 4 in manuscript also changed to a similar expression. A detailed discussion about the comparison of relationships has been added in section 4.1 as follows:

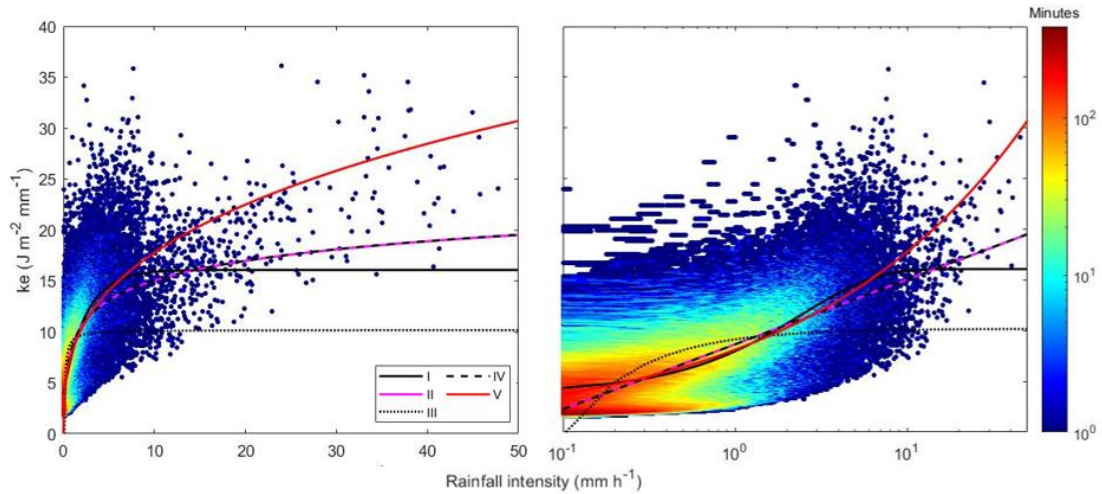


Figure 1 (new Figure 2 in manuscript). Minutes number per intensity class (x-axis) and ke class (y-axis) with five fitted $ke-I$ curves at Chilbolton station (2004–2013), plotted on linear (left) and logarithmic (right) intensity scales.

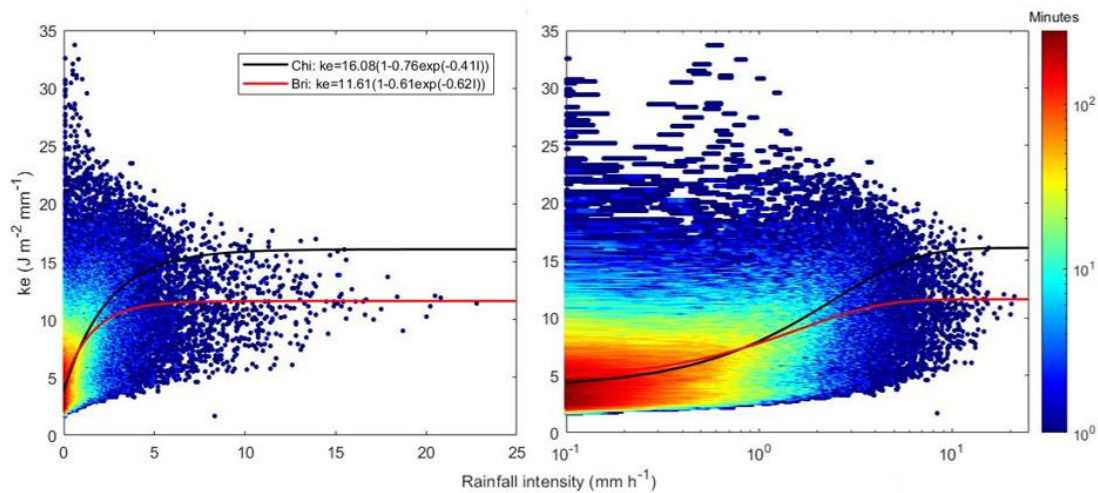


Figure 2 (new Figure 4 in manuscript). Minutes number per intensity class (x-axis) and ke class (y-axis) with fitted $ke-I$ curves at Bristol station (2015–2018), plotted on linear (left) and logarithmic (right) intensity scales.

“Figure 2 shows the $ke-I$ relationship and five fitted curves at Chilbolton station. It can be seen that the two logarithmic curves (Equation II and IV) invariably overlap. The logarithmic form has been used for a long time in USLE (Wischemier and Smith, 1978). It describes ke well at both low and high I , but does not have an upper limit. The power law curve (Equation V) can predict ke well at lower I but overestimates ke at high I . The exponent-based relationship (Equation I) is widely used in the literature and in forecast models such as RUSLE (Renard et al., 1997), which fits the data particularly well in Figure 2. Even though ke in exponential curve has a minimum value at very low I , it also should be noted that higher rainfall intensities are much more important in determining overall storm energy than lower intensities. Therefore, we adopted it here as the empirical formula to estimate rainfall erosivity in the UK.”

Point 4: The Discussion section is one of the most exciting parts of any study and preferably to be presented separately from the Results section. Add the Discussion section and compared the study finding with previous studies.

Response 4: Discussion part is mainly contained in the conclusion section. The following text has been added in the Section 5 to enrich the discussion:

“The reliability of the WRF model is heavily dependent on the model-driving initial data provided by mesoscale or global models and complicated scheme setting and parameter adjustment (Liu et al., 2013; Thompson and Eidhammer, 2014; Kumar et al., 2017). However, numerous uncertainties are observed in the parameterization of the WRF simulation, and the choice of microphysical schemes has a significant influence on the inverted DSD (Ćurić et al., 2009; Yang et al., 2019). Therefore, combining the DSDs obtained by an increasing number of disdrometers and the WRF model is valuable. For example, the Disdrometer Verification Network (DiVeN) in the UK (Pickering et al., 2019) started in Feb 2017 can be introduced to support and improve our estimation in future studies.”

“Soil erosion in the UK is dominated by water erosion ($10\text{--}30\text{ t km}^{-2}\text{ yr}^{-1}$), especially in areas with abundant rainfall in Scotland, where the soil loss rate is approximately 5–10 times that of dry areas (Duck, 1996). Thus, it is significant to estimate rainfall erosivity to elucidate the microphysical characteristics of rainfall and rainfall–soil interactions. Benaud et al. (2020) collated empirical soil erosion observations from UK-based studies into a geodatabase. However, there is a limitation that this database does not cover the entirety of the UK, especially the limited records in northern Scotland. In our future work, we propose to compare the soil loss database with our estimated soil loss using WRF DSD based rainfall erosivity and a soil erosion model (such as RUSLE). We believe that not only can we better analyze the impact of rainfall and rainfall erosivity on the UK soil loss, but also help to better understand microphysical rainfall–soil interactions to support the rational formulation of soil and water conservation planning.”

Benaud, P., Anderson, K., Evans, M., Farrow, L., Glendell, M., James, M. R., ... & Brazier, R. E. (2020). National-scale geodata describe widespread accelerated soil erosion. *Geoderma*, 371: 114378.

Ćurić, M., Janc, D., Vučković, V. and Kovačević, N. (2009). The impact of the choice of the entire drop size distribution function on Cumulonimbus characteristics. *Meteorologische Zeitschrift* 18(2): 207-222.

Duck, R. W. (1996). Regional variations of fluvial sediment yield in eastern Scotland. *Erosion and Sediment Yield: Global and Regional Perspectives: Proceedings of an International Symposium Held at Exeter, UK, IAHS*.

Kumar, P., Kishtawal, C. and Pal, P. (2017). Impact of ECMWF, NCEP, and NCMRWF global model analysis on the WRF model forecast over Indian Region. *Theoretical and Applied Climatology* 127(1-2): 143-151.

Liu, J., Bray, M. and Han, D. (2013). Exploring the effect of data assimilation by WRF - 3DVar for numerical rainfall prediction with different types of storm events. *Hydrological Processes* 27(25): 3627-3640.

Pickering, B. S., Neely III, R. R., & Harrison, D. (2019). The Disdrometer Verification Network (DiVeN): a UK network of laser precipitation instruments. *Atmospheric Measurement Techniques* 12: 5845-5861.

Thompson, G. and Eidhammer, T. (2014). A study of aerosol impacts on clouds and precipitation development in a large winter cyclone. *Journal of the Atmospheric Sciences* 71(10): 3636-3658.

Yang, Q., Dai, Q., Han, D., Chen, Y. and Zhang, S. (2019). Sensitivity analysis of raindrop size distribution parameterizations in WRF rainfall simulation. *Atmospheric Research* 228: 1-13.

Point 5: What about ground truthing validation of your results in the whole UK or using previous studies with experimental and in-situ data?

Response 5: Rainfall erosivity are difficult to measure, because they refer to erosive potential of rainfall, not the amount of soil erosion that rainfall specifically causes. In RUSLE, soil loss can be estimated by multiplying the rainfall erosivity factor (R-factor) by five other factors: soil erodibility (K-factor), slope length (L-factor), slope steepness (S-factor), crop type and management (C-factor), and supporting conservation practices (P-factor). For ground verification, we believe that disdrometer is the most accurate measurement instrument currently for rainfall erosivity estimation. Results derived by disdrometers are sufficient as a reference to support this study. Moreover, DiVeN you pointed out in Point 2 may be a great data source for ground verification in our future in-depth work.

Point 6: How much your study can be compared or can support the very recently published research entitled "National-scale geodata describe widespread accelerated soil erosion" <https://doi.org/10.1016/j.geoderma.2020.114378>. The latter publication can enrich the discussion part of the study.

Response 6: Thanks for your kind advice. As mentioned in the Point 5, rainfall erosivity and soil erosion caused by rainfall are completely different concepts. The publication you pointed out collected all readily available and empirically-derived soil erosion data from UK-based studies into a geodatabase. However, the database did not cover the entire UK completely. For instance, compared to England data, Scotland has very few soil erosion records in the database. Based on the analysis of existing records, authors found that there was a weak positive relationship between the total annual precipitation and soil erosion rates in some areas. We believe that putting the rainfall erosivity estimation based on WRF DSD into a soil erosion model (such as RUSLE) and estimating large-scale soil loss can enrich the UK soil loss database. In this way, not only can we better analyze the impact of rainfall and rainfall erosivity on UK soil loss, but also help to better understand microphysical rainfall–soil interactions to support the rational formulation of soil and water conservation planning.

The corresponding text has been added (see Point 4).

Point 7: Avoid using the abbreviation in the abstract and key points.

Response 7: Agreed and amended.

Point 8: Enrich the Figures and Tables captions, ensuring selfexplaining to the readers without referring to the main text and avoiding abbreviations.

Response 8: Agreed and amended.

1 **Estimation of rainfall erosivity based on WRF-derived raindrop size distributions**

2 Qiang Dai^{1,2}, Jingxuan Zhu¹, Shuliang Zhang¹, Shaonan Zhu³, Dawei Han² and Guonian Lv¹

3 ¹Key Laboratory of VGE of Ministry of Education, Nanjing Normal University, Nanjing, China.

4 ²Department of Civil Engineering, University of Bristol, Bristol, UK.

5 ³College of Geographical and Biological Information, Nanjing University of Posts and
6 Telecommunications, Nanjing, China

7 Corresponding author: Qiang Dai (qd_gis@163.com)

8 **Key Points:**

- 9 • ~~WRF-derived-r~~Rainfall kinetic energy derived from the Weather Research and
10 Forecasting model offers a novel way to estimate large-scale soil erosion.
- 11 • Annual rainfall and erosivity are not always positively correlated.
- 12 • Highest rainfall erosivity of UK occurs in the west coast area during 2013--2017.

13

14 Abstract

15 Soil erosion can cause various ecological problems, such as land degradation, soil fertility loss,
16 and river siltation. Rainfall is the primary water-driving force for soil erosion, and its potential
17 effect on soil erosion is reflected by rainfall erosivity that relates to the raindrop kinetic energy
18 (~~KE~~). As it is difficult to observe large-scale dynamic characteristics of raindrops, all the current
19 rainfall erosivity models use the function based on rainfall amount to represent the raindrops
20 kinetic energy~~KE~~. With the development of global atmospheric re-analysis data, numerical
21 weather prediction (~~NWP~~) techniques become a promising way to estimate rainfall kinetic
22 energy~~KE~~ directly at regional and global scales with high spatial and temporal resolutions. This
23 study proposed a novel method for large-scale and long-term rainfall erosivity investigations
24 based on the Weather Research and Forecasting (WRF) model, avoiding errors caused by
25 inappropriate rainfall–energy relationships and large-scale interpolation. We adopted three
26 microphysical parameterizations schemes (Morrison, WDM6, and Thompson aerosol-aware
27 ~~TAA~~) to obtain raindrop size distributions, rainfall kinetic energy~~KE~~ and rainfall erosivity,
28 with validation by two disdrometers and 304 rain gauges around the United Kingdom. Among
29 the three WRF schemes, Thompson aerosol-aware~~TAA~~ had the best performance compared with
30 the disdrometers at a monthly scale. The results revealed that high rainfall erosivity occurred in
31 the west coast area at the whole country scale during 2013–2017. The proposed methodology
32 makes a significant contribution to improving large-scale soil erosion estimation and for better
33 understanding microphysical rainfall–soil interactions to support the rational formulation of soil
34 and water conservation planning.

35

36 1 Introduction

37 Soil erosion has-plays a pivotal role in shaping the Earth’s physical landscape; however,
38 it can threaten both ecosystems and human societies (Alewell et al., 2015). Accurate
39 quantification of soil loss impact at large spatial scales is therefore important for developing
40 land-use planning and sustainable conservation practices (Bilotta et al., 2012). The soil erosion
41 rate is driven by a combination of factors, which-includinge rainfall, topography, soil
42 characteristics, land cover, and land management applications (Wischmeier and Smith, 1958;
43 Panagos et al., 2015b). Among these, rainfall is a driving force that accounts for a large

44 proportion of soil loss throughout most of the world (Panagos et al., 2015b). The erosive force of
45 rainfall with consequent runoff is represented as erosivity of rainfall. This, which is a crucial
46 factor for estimating soil loss in large-scale soil erosion models; for instance, the Universal Soil
47 Loss Equation (USLE (Wischmeier and Smith, 1978) or RUSLE (Renard et al., 1997)), Limburg
48 Soil Erosion Model (LISEM) (De Roo et al., 1996), and USLE-M (Kinnell and Risse, 1998).

49 Rainfall erosivity estimation involves the microphysical properties of rainfall and
50 rainfall–soil interactions on different time steps (Petan et al., 2010). Impact of rainfall, the main
51 mechanism driving the splashing of soil particles from the soil mass, which leads to soil erosion
52 through soil disintegration and mobilization, relies on the kinetic energy (KE) of raindrop
53 motions (Wischmeier and Smith, 1958; Wang et al., 2014). Robust measurement of raindrop size
54 and terminal velocity is vital for estimating and predicting rainfall erosivity. Many measurements
55 can be used to obtain these two parameters, including the stained paper or flour pellet methods
56 (Marshall and Palmer 1948; Wischmeier and Smith, 1958), high speed cameras (Jones, 1959;
57 Kinnell, 1981; McIsaac, 1990), and disdrometers (Petan et al., 2010; Angulo-Martinez et al.,
58 2012). Accurate measurements of raindrop size can be provided in all their methods, and
59 terminal velocity of raindrops can be further measured by video cameras and disdrometers.
60 Velocity can also be estimated as the function of raindrop diameter from the empirical
61 relationship (Beard, 1976; Atlas and Ulbrich, 1977; Uplinger, 1981; Van Dijk et al., 2002).
62 When using ground observations, rainfall KE can be estimated at a given site.

63 However, direct measurement of rainfall KE in a large area is difficult because it requires
64 considerable effort, as well as a dense network of expensive instruments that provide accurate
65 outputs (Fornis et al., 2005; Mikoš et al., 2006; Meshesha et al., 2016; Dai et al., 2017). Previous
66 studies have, therefore, mainly employed more readily accessible records like rainfall intensity,
67 and attempted to estimate rainfall KE from the empirical relationship of unit KE (*ke*) with
68 intensity (*ke–I*). Since Marshall and Palmer (1948) first observed a two-parameter exponential
69 relationship between drop size and intensity, several forms of *ke–I* mathematical expressions for
70 specific locations and climatic conditions have been proposed, including power-law (Park et al.,
71 1982; Meshesha et al., 2016), linear (Sempere-Torres et al., 1998; Nyssen et al., 2005),
72 polynomial (Carter et al., 1974), logarithmic (Wischmeier and Smith, 1978; Davison et al., 2005;
73 Meshesha et al., 2014), and exponential (Kinnell, 1981; Brown and Foster, 1987) relationships.
74 Among these, the exponential function has been preferentially used currently (Van Dijk et al.,

2002; Fornis et al., 2005; Petan et al., 2010; Sanchez-Moreno et al., 2012; Lim et al., 2015).
Accurate raindrop size distribution (DSD) measured by disdrometers is widely used to derive ke –
 I relationships (Angulo-Martínez et al., 2016; Meshesha et al., 2016). However, such empirically
derived formulas indicate that rainfall ke will increase infinitely with increasing intensity,
whereas studies (Rosewell, 1986; Angulo-Martínez et al., 2016; Meshesha et al., 2019) have
found that rainfall ke reaches an top value when intensity is around 70 mm h^{-1} (Hudson, 1963;
Wischmeier and Smith, 1978). More importantly, such a ke – I relationship only represents local
climate and precipitation microphysics, and is valid for such regions. There is great uncertainty
associated with rainfall erosivity estimation using this ke – I relationship in a large domain
(Angulo-Martínez and Barros, 2015), especially due to the poor spatial and temporal
predictability of the ke – I relationship. This has motivated researchers to directly calculate KE
based on large-scale DSD measurements.

Ground- and space-based radar can be used to obtain DSD parameters (Atlas et al., 1973;
Doelling et al., 1998). For example, the space-borne Dual-frequency Precipitation Radar (DPR)
radar containing Ku- and Ka-bands in the Global Precipitation Measurement (GPM) satellite
allows researchers to estimate the global three-dimensional spatial distribution of hydrometeors.
Unfortunately, ground dual-polarization radars are available in limited areas (Prigent, 2010) with
large uncertainties (Dai et al., 2019), and the GPM DPR instrument, which measures DSD with
daily or longer temporal resolutions, fail to capture a full storm and meet the requirement for
rainfall kinetic estimation. Mesoscale numerical weather prediction models, for instance, the
WRF model, can simulate microphysical cloud processes and predict the evolution of particle
size distribution through computationally feasible parametrization schemes (Dai et al., 2014;
Brown et al., 2016). DSD on the ground can be derived from the WRF model through
consideration of various physical processes, types of hydrometeor, and free degrees of size
distributions in hydrometeor. As such, a number of recent researches have investigated the
retrieval and uncertainty of DSD parameters by WRF (Gilmore et al., 2004; Ćurić et al., 2009;
Brown et al., 2016; Yang et al., 2019).

The WRF model runs with initial and boundary conditions using global reanalysis
datasets, such as those of the European Centre for Medium-range Weather Forecasts (ECMWF)
and National Centers for Environmental Prediction (NCEP). In other words, WRF-derived DSD
can be obtained for any given area with fine spatial and temporal resolutions rather than

106 traditional course linear interpolations. We therefore attempted to estimate rainfall erosivity for
 107 the entirety of the ~~whole~~ United Kingdom (UK) domain using WRF-derived DSD. For
 108 comparison, we also calculated interpolated traditional disdrometer-derived rainfall erosivity. To
 109 our knowledge, this work is the first attempt to take advantage of a numerical weather prediction
 110 model for estimating rainfall erosivity anywhere around the world. The current study contributes
 111 to the development of large-scale soil erosion estimation and provides a better comprehension of
 112 microphysical rainfall–soil interactions.

113 2 Methodology

114 2.1 Disdrometer-based rainfall KE estimation

115 KE dominates the ability of raindrops to separate soil particles. The KE (e , unit: J) of a
 116 raindrop with mass m (g) and terminal velocity v (m s^{-1}) is defined by:

$$e = \frac{1}{2} mv^2 \quad (1)$$

117 Assuming a spherical volume for every raindrop shape, the mass of a drop can be
 118 calculated from the cube of the diameter D (mm). Because instruments (e.g., disdrometers)
 119 generally sample drop size, the mean radius and falling velocity of the corresponding sampling
 120 drop-size class is-are used to represent D and v , expressed as D_i and v_i , respectively. In such
 121 cases, the e_i with any drop of a given class is given as:

$$e_i = \frac{1}{12} 10^{-6} \pi \rho v_i^2 D_i^3 \quad (2)$$

122 where ρ is the water density (g cm^{-3}). The sum of the KE of each individual raindrop within a
 123 given rain depth that hits a given area defines the total KE. The unit rainfall KE ke_t in the t^{th}
 124 minute ($\text{MJ ha}^{-1} \text{mm}^{-1}$) can be calculated as the sum of each drop KE in each size set, as follows:

$$ke_t = \frac{e_{sum}}{AP_t} = \frac{1}{AP_t} \sum_{i=1}^{ni} N_i e_i \quad (3)$$

125 where A represents the sample area of the sensor, P_t is rainfall depth at time t , and N_i is the drops
 126 number in class i . The instrument sums up the number of raindrops in each sampling class and
 127 produces the raindrop spectra for a time step. Here, we use the term ke to represent the

128 disdrometer-based KE estimated by DSD directly measured ~~directly~~ every minute. The terminal
 129 velocity of a raindrop can be estimated from its power law empirical relationship with raindrop
 130 diameter (Atlas and Ulbrich, 1977), with this considered more suitable for Chilbolton in the UK
 131 (Islam et al., 2012):

$$v_{Atl} = 3.78D_i^{0.67} \quad (4)$$

132 Thus, unit rainfall KE estimates per minute are obtained by replacing v_i in Eq. (2) with v_{Atl} .

133 The other form of rainfall KE is expressed at an event scale and represents the sum of the
 134 storm energy covering all time steps covering an event. The individual event energy (MJ ha^{-1}) is
 135 calculated as follows:

$$E = \sum_{t=1}^{nt} ke_t P_t \quad (5)$$

136 where P_t is the rainfall amount (mm) in the t^{th} minute and nt is the time steps number. Historical
 137 rainfall data are divided into wet and dry periods. A string of erosive rainfall storms ~~are~~is first
 138 extracted through the predefined rules. A continuous 6-h dry period interval was used to divide
 139 rainfall events (Hanel et al., 2016), following the “minimum dry-period duration” definition of a
 140 rainfall event (Bonta, 2004). Moreover, a rainfall amount of 12.7 mm was set as the threshold to
 141 filter effective rainfall events (Renard et al., 1997).

142 Rainfall KE is obtained for a given site based on size and velocity of raindrops. When
 143 disdrometer data are ~~absenee~~absent, energy can be estimated from empirical relationships using
 144 rainfall intensity I (mm). Five commonly used functions (including exponential, logarithmic,
 145 power law, and inverse proportion) have been mentioned in Section 1. Taking the exponential
 146 form as an example, the rainfall KE at any location can be estimated as:

$$E_{\max} = e_{\max}(1 - ae^{-bI}) \quad (6)$$

147 where e_{\max} is the mean maximal value of energy measured under high rainfall intensity, and a
 148 and b are coefficients modeling the equation curve. Here, minimum KE can be determined by
 149 parameters a and e_{\max} together, while the overall shape of the curve is modeled by parameter b .

150 2.2 WRF-based rainfall KE estimation

151 Differing from disdrometer measurements, the complete DSD cannot be obtained from
 152 the WRF model. Instead, the DSD of the microphysical parameterization (MP) scheme is
 153 handled with a constrained-gamma distribution model, which is defined as:

$$N(D) = N_0 D^\mu e^{-\lambda D} \quad (7)$$

154 where N_0 , μ , and λ are the intercept, shape, and slope parameters of the DSD. In terms of
 155 double-moment bulk schemes, N_0 and λ can be abstracted from the number concentration N and
 156 predicted mixing ratio q , as shown below:

$$N_0 = \frac{N \lambda^{\mu+1}}{\Gamma(\mu + 1)} \quad (8)$$

$$\lambda = \left[\frac{c M (\mu + d + 1)}{q \Gamma(\mu + 1)} \right]^{\frac{1}{d}} \quad (9)$$

157 c and d are the assumed power-law coefficients between diameter and mass ($m = cD^d$), and Γ
 158 represents the function in gamma form (Morrison et al., 2009). The value of the shape parameter
 159 μ ($\mu = 0$) in double-moment schemes is fixed, except for the WRF double-moment 6-class
 160 (WDM6) schemes, following gamma distribution, which defined $\mu = 1$ (Jung et al., 2010;
 161 Johnson et al., 2016).

162 Because DSD retrieval is sensitive to MPs (Cintineo et al., 2014; Morrison et al., 2015),
 163 the WRF model this study adopted completely or partially three types of double-moment cloud
 164 MP schemes. The Morrison double-moment scheme involves the number concentrations and
 165 mixing ratios of multiple hydrometeors (Morrison et al., 2009). Moreover, the WDM6 scheme
 166 further considers a prognostic factor to estimate and predict the cloud condensation nuclei (CCN)
 167 number concentration (Hong et al., 2010; Lim and Hong, 2010). Finally, the Thompson aerosol-
 168 aware (TAA) scheme can predict both ice nuclei (IN) and CCN number concentrations
 169 (Thompson and Eidhammer, 2014).

170 The DSD parameters were thus obtained under the three WRF MPs. For theoretical DSD,
 171 ke estimates per minute were obtained by integration of the full raindrop size spectrum using:

$$ke'_t = \frac{1}{AR_t} \int_0^\infty N(D) \frac{1}{12} 10^{-6} \pi \rho v_i^2 D_i^3 dD \quad (10)$$

172 For the WRF-derived DSD covering the whole study area, there was no need to construct
 173 a ke - I relationship to interpolate KE in ungauged areas. The WRF-based rainfall KE under storm
 174 event scale is thus given as:

$$E_w = \sum_{t=1}^{nt} ke'_t P_t \quad (11)$$

175 2.3 Rainfall erosivity estimation

176 Most storm events have relatively low intensities and KEs with occasional peaks, based
 177 on the disdrometer DSD data used to evaluate the rainfall ke - I function. Proper estimation of
 178 rainfall erosivity potential should consider total KE over a long period. The rainfall erosivity
 179 factor (or R-factor) is calculated by a multi-annual average of the total storm erosivity index
 180 (Wischmeier and Smith, 1958; Van Dijk et al., 2002), while annual rainfall erosivity R can be
 181 obtained using:

$$R = \sum_{m=1}^M (EI_{30})_m \quad (12)$$

182 where M is the total number of erosive events within a year. $(EI_{30})_m$ are total rainfall kinetic
 183 energy and maximum 30-min rainfall intensity recorded within 30 consecutive minutes (unit:
 184 mm h^{-1}), respectively, for the m^{th} event.

185 Wischmeier and Smith (1958) first proposed the use of EI_{30} , as the rainfall erosivity for
 186 each event, based on research data from many sources. I_{30} was calculated to have higher
 187 relevance to soil erosion than maximum 5-min, 15-min, or 60-min rainfall intensities
 188 (Wischmeier and Smith, 1958). The calculation of EI_{30} initially uses recording-rain gauge data to
 189 divide continuous rainfall into time periods with equal rainfall intensity. ~~Because~~ Though rainfall
 190 measurements with high temporal resolutions are required, ~~it is~~ but difficult to obtain them from
 191 general rainfall measurements. ~~Therefore,~~ Therefore, short time equal-interval rainfall data with higher
 192 accuracy over multiple years are preferred for estimating EI_{30} . For example, Xie et al. (2016)
 193 used 1-min rainfall data instead of recording-rain gauge records. For coarse-resolution, equally

194 spaced data, researchers have proposed a conversion factor to reduce bias error (Weiss, 1964;
195 Williams and Sheridan, 1991).

196 The rainfall erosivity can be derived from rainfall KE. It plays a main dynamic role in
197 USLE/RUSLE, representing the potential for soil erosion caused by rainfall. To distinguish the
198 disdrometer- and WRF-derived rainfall erosivity in this study, we use the terms R_D and R_W ,
199 respectively.

200 2.4 Evaluation methods

201 Because there is no direct way to measure rainfall erosivity across a large area, it is
202 difficult to validate outcomes using observations. However, R_D is considered to be relatively
203 accurate due to its specific measurement of raindrops. We therefore assumed that R_W values were
204 accurate if it closely matched R_D of a given location. A long-term comparison of R_W and R_D at
205 disdrometer stations was thus conducted to evaluate the validity of R_W .

206 Three indicators were introduced for the evaluation: Pearson's correlation coefficient,
207 mean absolute error (MAE), and coefficient of determination (R^2) (Borrelli et al., 2017). Pearson
208 correlation coefficient is an index used to evaluate the linear correlation between two variables,
209 and is defined as follows:

$$Pearson = \frac{n \sum R_{D_i} \sum R_{W_i} - \sum R_{D_i} \sum R_{W_i}}{\sqrt{n \sum R_{D_i}^2 - (\sum R_{D_i})^2} \sqrt{n \sum R_{W_i}^2 - (\sum R_{W_i})^2}} \quad (13)$$

210 where n is the number of variable samples. Because this correlation cannot reveal the absolute
211 bias of rainfall erosivity values, the MAE was also used; this is defined as:

$$MAE = \frac{\sum |R_{W_i} - R_{D_i}|}{n} \quad (14)$$

212 R^2 is an indicator to assess the fit of the trend line, expressed as the ratio of the variance
213 in the dependent variable predicted from the independent variable. It measures the extent to
214 which the model replicates observations based on the proportion of the results interpreted by the
215 model to the total change, written as:

$$R^2 = 1 - \frac{SS_{res}}{SS_{tot}} \quad (15)$$

216 where SS_{res} is the sum of squares of residuals between two variables, and SS_{tot} is the total sum of
217 squares.

218 **3 Study area and data sources**

219 The whole of the UK was set as the experimental area for investigating rainfall erosivity
220 estimation. The UK consists of mostly lowland terrain, with a maximum elevation of 1345 m.
221 Water and wind are the most significant forces of soil erosion in the UK, ~~and~~. Together, they
222 cause approximately 2.2 million tons of topsoil to be eroded annually, seriously affecting soil
223 productivity, water quality, and aquatic ecosystems through siltation of watercourses (EA, 2004).
224 According to the Environmental Agency, the total cost of soil erosion in the UK is approximately
225 \$88 million each year, including an agricultural production loss of \$17.6 million (O'Neill, 2007).
226 More importantly, the changing climate may exacerbate the degree of erosion. For example,
227 hotter, drier climates make soils more susceptible to wind erosion, and intense storms increase
228 rainfall erosivity (Defra, 2009). Studies of water erosion in England and Wales (Morgan, 1985;
229 Evans, 1990) have found that loose soils (especially sand), such as the soils found in Shropshire
230 and Herefordshire in Wales, are more susceptible to water erosion. In a study of rainfall erosion
231 in Europe, Panagos et al. (2015a) found that the humid Atlantic climate results in highly variable
232 rainfall erosivity, such as higher R-factor values in western England and lower values in the
233 eastern UK.

234 The gauge datasets used are from the land surface and marine surface measurements
235 datasets (data availability: 1853–present) provide by the UK Met Office. A network of rain
236 gauges covering 304 stations across the whole UK observes continuous rainfall data in hours
237 (Figure 1). The base data of most stations comprises the times of each tip (0.2 mm per tip),
238 converted into 1-h rain accumulations. The rainfall observations are not always valid for each
239 hour at each station. The hourly grid-based rainfall maps are then calculated based on ordinary
240 kriging interpolation of rain gauge network data to obtain the spatial distribution of rainfall for
241 each time step, as inputs for rainfall erosivity estimation. This wide-range-use geostatistical
242 approach can account for both the distance and pairwise spatial relationship between points

243 through variograms. The precipitation interpolation method uses sample gauge points taken at
244 different locations and creates a continuous surface to achieve an accurate spatial variation
245 estimation of rainfall patterns.

246 We used data from two disdrometers in southern England. The first was Chilbolton
247 station (51°08'N, 1°26'W), with an impact-type Joss–Waldvogel disdrometer (JWD) mainly
248 used to compute rainfall erosivity. It can measure drop sizes from 0.3 to 5.0 mm in 127 bins. The
249 sampling period and collector area were 10 s and 50 cm², respectively. Data were available for
250 April 2003 to July 2018. The second was the University of Bristol station (51°27'N, 2°36'W),
251 with an OTT Parsivel² disdrometer (OPD). Data were available for November 2015 to December
252 2018. This disdrometer subdivides particles into appropriate classes and has a nominal cross-
253 sectional area of 54 cm². The 10-s period measurement data from the two disdrometers were
254 averaged into a 1-min period to filter out time variations (Montopoli et al., 2008; Islam et al.,
255 2012; Song et al., 2017).

256 Meteorological data comes from the ERA-Interim dataset, a global atmosphere re-
257 analysis product, generated by the ECMWF. For the scientific community, ERA-Interim is
258 considered to be one of the most important atmospheric datasets, with its ~~data~~-~~data~~-rich period
259 available since 1979 and updated in current time (Dee et al., 2011). The Integrated Forecasting
260 System released in 2006 contains a 12-h analysis window derived 4-D variational analysis,
261 driving the data assimilation system to generate ERA-Interim. The dataset covers 60 vertical
262 classes of approximately 80 km from the ground to 0.1 hPa. The Gridded Binary format is used
263 to store data for three months in a separate file. A data processing scheme was established to
264 collect and retrieve ERA-Interim data of each rainfall event.

265 The rain gauge and Chilbolton disdrometer datasets can be obtained from British
266 Atmospheric Data Centre in National Centre for Atmospheric Science research center (MO,
267 2012). ERA-Interim data can be obtained from the ECMWF Public Dataset website
268 (<https://apps.ecmwf.int/>). Considering the availability of the above datasets and model
269 requirements, we mainly used data covering the period 2004–2017.

270 4 Results

271 4.1 Empirically derived rainfall erosivity estimation

272 To evaluate the R_w , the raindrop spectrum collected by the Chilbolton station disdrometer
273 is used to estimate rainfall KE first. The key in estimating rainfall KE by disdrometer lies ~~on~~in
274 building an empirical relationship between rainfall amount and KE. We used DSD measurements
275 from 2004 to 2013 to establish five empirical relationships between unit rainfall kinetic energy
276 (ke) and intensity (I) (Table 1), and used 2014–2017 data for the ~~cross~~cross-validation. It can be
277 seen from Table 1 that the inverse proportional relationship (Equation III~~-in Table 1~~) had the
278 worst performance, in that both the calibration and validation R^2 values were < 0.3 . The values
279 of the other equations were > 0.48 , among which the exponential formula (Equation I~~-in Table 1~~)
280 had the highest calibration R^2 (0.50) and validation R^2 (0.45), respectively. In addition, the
281 power law formula (Equation V~~-in Table 1~~) showed a similar performance to the exponential
282 formula at rainfall intensities $< 5 \text{ mm h}^{-1}$. However, the power law formula also had a
283 continuously increasing trend, which may not be suitable for high-intensities. Figure 2 shows the
284 ke - I relationship and five fitted curves at Chilbolton station. It can be seen that the two
285 logarithmic curves (Equation II and IV) invariably overlap. The logarithmic form has been used
286 for a long time in USLE (Wischemier and Smith, 1978). It describes ke well at both low and high
287 I , but does not have an upper limit. The power law curve (Equation V) can predict ke well at
288 lower I but overestimates ke at high I . The exponent-based relationship (Equation I) is widely
289 used in the literature and in forecast models such as RUSLE (Renard et al., 1997), which fits the
290 data particularly well in Figure 2. Even though ke in exponential curve has a minimum value at
291 very low I , it also should be noted that higher rainfall intensities are much more important in
292 determining overall storm energy than lower intensities. Therefore, we adopted it here as the
293 empirical formula to estimate rainfall erosivity in the UK.~~Figure 2 shows the fitted relationship~~
294 ~~of ke - I based on exponential regression.~~

295 ~~The exponent based relationship is widely used in the literature and in forecast models~~
296 ~~such as RUSLE (Renard et al., 1997). We therefore adopted it here as the empirical formula to~~
297 ~~estimate rainfall erosivity in the UK.~~

298 Based on rainfall KE, the point R_D can be obtained at a disdrometer location. In the
299 current study, we established a method to estimate the ~~R -factor~~ using 60-min rainfall data. EI_{30}

300 obtained from 1-min DSD data was considered as the standard *R-factor* at Chilbolton Station.
301 Hourly rain gauge data at the same location were used to calculate $(EI_{30})_{60}$, which refers to EI_{30}
302 calculated from 60-min data. The regression relationship between EI_{30} and $(EI_{30})_{60}$ was then
303 established. The $(EI_{30})_{60}$ of each month, obtained from the 60-min rainfall data of the Chilbolton
304 Station rain gauge in 2004–2013, was calculated. The regression relationship between the
305 monthly sum of $(EI_{30})_{60}$ and the standard monthly EI_{30} from DSD was calculated to obtain a
306 coefficient of 1.836. Rainfall erosivity can subsequently be calculated by multiplying $(EI_{30})_{60}$ by
307 the coefficient.

308 Beyond assuming that the disdrometer-derived *ke-I* relationship can be applied to a
309 whole study area; point rainfall measurements must be interpolated to obtain areal rainfall values
310 in traditional rainfall erosivity estimation. We obtained 60-min rainfall data from 304 rain gauges
311 around the UK from 2004 to 2017. Note that not all rain gauges were available for the whole
312 period (available gauges each year are indicated in Figure 3). We used the ordinary kriging
313 interpolation method to obtain the spatial distribution of rainfall for each time step. This wide-
314 range-use geostatistical approach can account for both the distance and pairwise spatial
315 relationship between points through variograms. Figure 3 shows the results of annual rainfall
316 (*Rain*), annual rainfall kinetic energy (*E*), and annual rainfall erosivity (*R*) for different years.
317 The distribution trends of *Rain*, *E*, and *R* were similar, and ~~were~~ positively correlated except for
318 certain locations or periods. For instance, in 2013, *Rain* in the northwestern UK decreased from
319 west to east, while *E* and *R-factor* decreased from south to north; furthermore, areas with large *E*
320 and *R* values in southeastern UK could not be directly observed from the rain map.

321 The key concern in traditional rainfall erosivity estimation is the spatial predictability of
322 the *ke-I* relationship. To verify the regional reliability of this relationship, we used data from a
323 newer disdrometer located at the University of Bristol, approximately 87 km from Chilbolton
324 Station. The validation data at Bristol Station discontinuously covered the period 2016–2019.
325 Figure 4 shows the exponential relationship of *ke-I* at Bristol station, which differed
326 substantially from that based on data from Chilbolton station. A comparison of the modeled and
327 observed event rainfall erosivity is shown in Figure 5. The modeled erosivity of rainfall event
328 was not consistent with the observed event rainfall erosivity. The linear regression coefficient
329 between these values was > 1.2 , which was the result of the low *ke* for Bristol Station, and R^2

330 was < 0.85, indicating ~~large-considerable~~ uncertainty associated with disdrometer-based rainfall
331 erosivity estimation.

332 In summary, the point rainfall erosivity estimated by disdrometer is considered to be
333 accurate compared to other methods. However, a large-scaled rainfall erosivity through a simple
334 interpolation of rainfall KE is subjected to a ~~large-significant~~ uncertainty. In the following
335 analysis, the point R_D is used to appraise the performance of ~~the~~ proposed WRF-based estimated
336 method, and the R_D in the whole UK is only be used for a general comparison of spatial and
337 temporal distribution of rainfall erosivity.

338 4.2 Rainfall and DSD estimation by WRF

339 We used the WRF model ver. 3.8, which has an Advanced Research WRF dynamical
340 core, to downscale the ERA-Interim reanalysis data. The double-nested domain configuration
341 used in the WRF model was centered at 55°19'N, 2°21'W and applied at a downscaling ratio of
342 1:5, a finest grid of 5 km, and a temporal resolution of 1 h. Table 2 lists the detailed parameters
343 used in this domain configuration. With the top pressure level set at 50 hPa in each, both
344 domains include 28 vertical levels. To obtain favorable initial weather conditions, the model ran
345 continuously to obtain five years of WRF simulation results.

346 Simulations were performed using three different bulk double moment MPs: the
347 Morrison (Morrison et al., 2009), WDM6 (Hong et al., 2010; Lim and Hong, 2010) and TAA
348 (Thompson and Eidhammer, 2014) schemes. All three can predict the number concentration and
349 hydrometeors mixing ratio ~~for~~ each time step. The WDM6 scheme also predicts the number
350 concentration of CCN (Hong et al., 2010; Lim and Hong, 2010), while the TAA scheme are able
351 to predict both IN and CCN number concentrations (Thompson and Eidhammer, 2014).
352 Additionally, other physical parameterizations include the Dudhia shortwave radiation scheme
353 (Dudhia, 1989), Mellor–Yamada–Janjic planetary boundary layer scheme (Janjić, 1994), RRTM
354 longwave radiation scheme (Mlawer et al., 1997), the Noah land-surface model (Ek et al., 2003),
355 and the Kain–Fritsch cumulus scheme (Kain, 2004),.

356 The median volume diameter parameter (D_0) and generalized intercept parameter (N_w)
357 are generally used in ~~the~~ DSD model of WRF (Islam et al., 2012).

$$N_w = \frac{N_0 D_m^\mu}{f(\mu)} \quad (16)$$

$$f(\mu) = \frac{6(4 + \mu)^{\mu+4}}{4^4 \Gamma(\mu + 4)} \quad (17)$$

358 where D_m is the mass-weighted mean diameter. The $f(\mu)$ is a function of the shape parameter μ .
 359 The parameter μ is assumed as zero or one (based on microphysical scheme configuration) in
 360 WRF. Figure 6 displays the spatial distribution of D_0 and generalized intercept parameter N_w for
 361 a given day with rainfall countrywide (January 10, 2013). D_0 and N_w had similar patterns, and
 362 were mainly distributed across the southwestern and northeastern UK. The white strip in the
 363 middle of Figure 6 represents an area that received no rain. However, the three MPs yielded large
 364 differences; D_0 of MP-TAA was the highest among three MPs, whereas N_w of MP-WDM6 was
 365 much-significant larger than the others. In addition, D_0 and N_w did not consistently show a
 366 positive correlation. The different MP estimation results underscore the complexity of the
 367 rainfall process, which is the reason we estimated rainfall KE using WRF schemes instead of
 368 traditional formulas.

369 4.3 Comparison of WRF- and disdrometer-derived rainfall erosivity at Chilbolton station

370 With the WRF-based rainfall intensity and DSD estimations, rainfall erosivity was
 371 derived using Equations (10)–(12). Hereafter, this is referred to as R_w , which is further
 372 distinguished based on the three MP schemes used: $R_{w-Morrison}$, R_{w-WDM6} , and R_{w-TAA} . Figure 7
 373 compares disdrometer- and WRF-derived monthly rainfall erosivity estimations at Chilbolton
 374 sStation for the period 2014–2017. The general patterns of the four rainfall erosivity values were
 375 similar. $R_{w-Morrison}$ tended to be larger than R_D in some months, whereas R_{w-TAA} matched the R_D
 376 value relatively well for smaller values. Because WRF data were taken from a 2- \times -2-km grid
 377 around Chilbolton sStation, there was a spatial error in addition to the systematic error of
 378 estimating rainfall erosivity. Based on the four-year data, the study area is rainy throughout the
 379 year with little R monthly, or seasonal patterns change (Figure 8), influenced by the temperate
 380 oceanic climate. Figure 8 also indicated that through the perspective of monthly average results,
 381 R_{w-WDM6} values are low, R_{w-TAA} has a good similarity with low R_D , and $R_{w-Morrison}$ is the closest to
 382 R_D in value.

383 Table 3 shows the correlation indicator results between monthly R_D and the three types of
384 R_W at Chilbolton station. The Pearson correlation coefficients generally exceeded 0.7, supporting
385 the potential utility of WRF-based estimation. In terms of MAE, R_{W-TAA} had the best performance
386 (6.51), whereas $R_{W-Morrison}$ and R_{W-WDM6} showed slightly worse performance (approximately 8).
387 Among the three schemes, R_{W-TAA} had the best fit with R_D . The indicators and comparison results
388 suggest that the deviations in results need to be considered; therefore, a method of bias
389 elimination is ~~therefore~~ described in Section 4.4.

390 4.4 R_W estimation for the whole UK

391 The R_W at Chilbolton station showed obvious systematic deviations compared with the
392 disdrometer-derived results (see Section 4.2 and 4.3). ~~A~~sSimple bias correction was therefore
393 applied to adjust the individual storm KE estimations of R_W . The biases from dividing average
394 $R_{W-Morrison}$, R_{W-WDM6} , and R_{W-TAA} by average R_D during 2014-2017 were 0.55, 0.20, and 0.36,
395 respectively.

396 The rainfall erosivity distribution for the whole UK was then obtained. Figure 98 shows
397 the distribution of R_W at the annual scale covering the period 2013–2017. The pattern of the
398 rainfall erosivity maps showed a general regional-dominant characteristic. For example, it
399 always decreased from west to east, predominantly shaped by orography. Affected by the
400 prevailing westerly winds, there was abundant rainfall in the western and northern mountains, as
401 indicated by high rainfall KE values in these regions. In addition, among the study years, 2014
402 and 2015 showed higher national rainfall erosivity, with a large range in the west coast area.

403 Figure 9-10 shows the average R distribution for 2013–2017 estimated by rain gauges and
404 WRF MPs. WRF grids could cover all regions in the UK evenly, offering more detailed erosivity
405 results, especially in the mountainous northwestern region. Here, values of average R map
406 calculated by rain gauges were much higher than three types of R_W , although they all have R
407 decreased from west to east. Noted that $ke-I$ empirical equation at Chilbolton station used in the
408 whole UK, will not always be accurate in regions with different rainfall characteristics. In terms
409 of R_W results, the three MPs obtained the same spatial pattern in rainfall erosivity, where R_{W-WDM6}
410 yielded the greatest geographical difference. It is clear that the proposed WRF-based estimated
411 method can capture more details of the spatial change of rainfall erosivity ~~eompares~~ compared
412 with the traditional disdrometer-based method.

413 The highest rainfall erosivity regions in the UK are concentrated in the mountainous
414 areas along the western coast, related to their rainfall system. The moist air brought by the
415 prevailing westerly wind from the Atlantic Ocean moves from west to east across the UK and
416 rises when it encounters the mountains of western England. Therefore, the mountainous regions
417 along the UK western coast have the highest rainfall amount and rainfall erosivity in the UK. In
418 addition, western Scotland is under the subpolar oceanic climate, which enhances its humidity.
419 On the contrary, eastern Scotland and northeastern England are more likely to expose continental
420 polar air mass, which brings dry and cold air and lower rainfall erosivity.

421 To evaluate the change in rainfall erosivity with time in the UK, the average value of all
422 the WRF grids covering the whole UK was calculated over 2013–2017 (Figure ~~10~~11). The
423 average R_W trends of $R_{W-Morrison}$ and R_{W-TAA} were similar, both increasing from a minimum in
424 2013 to a maximum in 2014, and then gradually decreasing from 2014 to 2017. The red line in
425 Figure ~~10~~11 indicates a series of mean values of the three MPs results, which varied from
426 36,782 to 51,600 MJ mm ha⁻¹ h⁻¹ y⁻¹ (mean: 43,216 MJ mm ha⁻¹ h⁻¹ y⁻¹).

427 The maximum values for $R_{W-Morrison}$ and R_{W-TAA} occurred in 2014, whereas that of R_{W-WDM6}
428 occurred in 2015. A sequence of extreme weather events occurred in the UK in 2014, including
429 major winter storms in late January to mid-February, which caused widespread flooding and
430 other economic losses, and greatly increased rainfall erosivity that year. However, the gauge-
431 based interpolation map shows the average annual rainfall amount for the years 2013–2017 were
432 884.9, 1014.0, 1008.5, 894.9, and 937.3 mm, respectively. The large rainfall erosivity difference
433 between 2014 and 2015, and the two years with similar rainfall amount, indicates that much
434 rainfall erosion occurs during the rainfall events of high intensity instead of simply high rainfall
435 amount. A mMore notable variation pattern of rainfall erosivity may be found with longer
436 simulation. The strength of the proposed method lies on its ability to estimate large covering and
437 long-term rainfall erosivity.

438 **5 Discussion and cConclusions**

439 This study presented a novel method for large-scale rainfall KE and erosivity estimation
440 based on high-high-resolution, WRF-derived DSDs. Three microphysical parameterizations
441 schemes (Morrison, WDM6, and Thompson aerosol-aware [TAA]) were designed to obtain
442 raindrop size distributions, rainfall KE and rainfall erosivity at-for the whole-entire of the UK

443 ~~scale~~ covering the period of 2013–2017. With validation ~~by~~from the long-term observations of
444 a disdrometer, the WRF-based rainfall erosivity ~~showed~~exhibited an acceptable performance at
445 Chilbolton station. Among the three WRF schemes, TAA exhibited the most superior
446 ~~performanced best~~ and was recommended for ~~the~~ future investigation. The results revealed that
447 high rainfall erosivity occurred in the west coast area ~~in~~of the UK. Compared with the
448 traditional empirical method, the proposed method can explain rainfall erosivity from a
449 microphysical perspective, and reflect more spatial variation ~~due to~~because of changes in rainfall
450 KE at the whole-country scale. Therefore, the development of a numerical weather prediction
451 model ~~therefore~~ offers an opportunity to better understand rainfall erosivity directly from its true
452 definition. More importantly, because the WRF model is able to be driven by the global
453 reanalysis data to obtain large-scale rainfall kinetic information, the proposed scheme can be
454 easily applied to other regions, especially in ungauged areas.

455 Although an acceptable rainfall erosivity estimation is obtained using the WRF model,
456 some uncertainties associated with it cannot be ignored. For example, as the MPs of WRF were
457 closely related to DSD, improper determination of MPs will introduce additional uncertainty.
458 The marked discrepancy among the three schemes (especially between Morrison and the others)
459 in this study underscored the possible uncertainty associated with R_w . The reliability of the WRF
460 model is heavily dependent on the model-driving initial data provided by mesoscale or global
461 models and complicated scheme setting and parameter adjustment (Liu et al., 2013; Thompson
462 and Eidhammer, 2014; Kumar et al., 2017). However, numerous uncertainties are observed in the
463 parameterization of the WRF simulation, and the choice of microphysical schemes has a
464 significant influence on the inverted DSD (Ćurić et al., 2009; Yang et al., 2019). Therefore,
465 combining the DSDs obtained by an increasing number of disdrometers and the WRF model is
466 valuable. For example, the Disdrometer Verification Network (DiVeN) in the UK (Pickering et
467 al., 2019) started in Feb 2017 can be introduced to support and improve our estimation in future
468 studies. Moreover, the measurement error by disdrometer may also contaminate the evaluation
469 process. For example, when comparing the observed raindrop velocities based on the
470 disdrometer at Bristol station with their empirical values, we observed a dispersion of raindrops,
471 with a number of drops showing significant deviations. This velocity distribution resulted in ~~an~~
472 uncertainty in ke estimation.

473 Soil erosion in the UK is dominated by water erosion (10–30 t km⁻² yr⁻¹), especially in
474 areas with abundant rainfall in Scotland, where the soil loss rate is approximately 5–10 times that
475 of dry areas (Duck, 1996). Thus, it is significant to estimate rainfall erosivity to elucidate the
476 microphysical characteristics of rainfall and rainfall–soil interactions. Benaud et al. (2020)
477 collated empirical soil erosion observations from UK-based studies into a geodatabase. However,
478 there is a limitation that this database does not cover the entirety of the UK, especially the
479 limited records in northern Scotland. In our future work, we propose to compare the soil loss
480 database with our estimated soil loss using WRF DSD based rainfall erosivity and a soil erosion
481 model (such as RUSLE). We believe that not only can we better analyze the impact of rainfall
482 and rainfall erosivity on the UK soil loss, but also help to better understand microphysical
483 rainfall–soil interactions to support the rational formulation of soil and water conservation
484 planning.

485 In addition, other sources of uncertainty, such as temporal downscaling of rainfall and
486 point-to-area representative error by WRF, may introduce further uncertainty. ~~This~~ ~~which~~
487 should be put in perspective of future work. It is expected that ~~more~~ ~~further~~ exploration of
488 research areas with different climatic and geographical characteristics would help us to establish
489 a greater degree of accuracy on this matter.

490 **Author contributions**

491 QD and JZ carried out the experiments, analyzed the data, and prepared the manuscript
492 with contributions from all the co-authors. SLZ modified the text and provided financial support.
493 SNZ carried out quality checks of WRF. GL and DH principally conceived the idea and design
494 of the study.

495 **Competing interests**

496 The authors declare that they have no conflict of interest.

497 **Acknowledgments**

498 This work was supported by the National Natural Science Foundation of China (Nos.
499 41871299 and 41771424), and the National Key R & D Program of China (Nos.
500 2018YFB0505500, 2018YFB0505502). The authors acknowledge the British Atmospheric Data

501 Centre and the European Centre for Medium-range Weather Forecasts as the sources of data used
502 in the study.

503 The rain gauge datasets and Chilbolton disdrometers were sourced from the Met Office
504 Integrated Data Archive System (MIDAS). Both datasets are available from the NCAS British
505 Atmospheric Data Centre (<http://archive.ceda.ac.uk/>). The ERA-Interim data driving the WRF
506 model can be downloaded from the ECMWF Public Datasets web interface
507 (<https://www.ecmwf.int/>).

508 **References**

509 Alewell, C., Egli, M. and Meusburger, K. (2015). An attempt to estimate tolerable soil erosion
510 rates by matching soil formation with denudation in Alpine grasslands. *Journal of Soils and*
511 *Sediments* 15(6): 1383-1399.

512 Angulo-Mart ínez, M. and Barros, A. (2015). Measurement uncertainty in rainfall kinetic energy
513 and intensity relationships for soil erosion studies: An evaluation using PARSIVEL disdrometers
514 in the Southern Appalachian Mountains. *Geomorphology* 228: 28-40.

515 Angulo-Mart ínez, M., Beguer á, S. and Kysel ý, J. (2016). Use of disdrometer data to evaluate the
516 relationship of rainfall kinetic energy and intensity (KE-I). *Science of the Total Environment* 568:
517 83-94.

518 Angulo-Martinez, M., Beguer á, S., Navas, A. and Machin, J. (2012). Splash erosion under
519 natural rainfall on three soil types in NE Spain. *Geomorphology* 175: 38-44.

520 Atlas, D., Srivastava, R. and Sekhon, R. S. (1973). Doppler radar characteristics of precipitation
521 at vertical incidence. *Reviews of Geophysics* 11(1): 1-35.

522 Atlas, D. and Ulbrich, C. W. (1977). Path-and area-integrated rainfall measurement by
523 microwave attenuation in the 1–3 cm band. *Journal of Applied Meteorology* 16(12): 1322-1331.

524 Beard, K. V. (1976). Terminal velocity and shape of cloud and precipitation drops aloft. *Journal*
525 *of the Atmospheric Sciences* 33(5): 851-864.

526 [Benaud, P., Anderson, K., Evans, M., Farrow, L., Glendell, M., James, M. R., ... & Brazier, R. E.](#)
527 [\(2020\). National-scale geodata describe widespread accelerated soil erosion. *Geoderma*, 371:](#)
528 [114378.](#)

529 Bilotta, G., Grove, M. and Mudd, S. (2012). Assessing the significance of soil erosion.
530 Transactions of the Institute of British Geographers 37(3): 342-345.

531 Bonta, J. (2004). Development and utility of Huff curves for disaggregating precipitation
532 amounts. Applied Engineering in Agriculture 20(5): 641.

533 Borrelli, P., Robinson, D. A., Fleischer, L. R., Lugato, E., Ballabio, C., Alewell, C., Meusburger,
534 K., Modugno, S., Schütt, B. and Ferro, V. (2017). An assessment of the global impact of 21st
535 century land use change on soil erosion. Nature Communications 8(1): 1-13.

536 Brown, B. R., Bell, M. M. and Frambach, A. J. (2016). Validation of simulated hurricane drop
537 size distributions using polarimetric radar. Geophysical Research Letters 43(2): 910-917.

538 Brown, L. and Foster, G. (1987). Storm erosivity using idealized intensity distributions.
539 Transactions of the ASAE 30(2): 379-386.

540 Carter, C. E., Greer, J., Braud, H. and Floyd, J. (1974). Raindrop characteristics in south central
541 United States. Transactions of the ASAE 17(6): 1033-1037.

542 Cintineo, R., Otkin, J. A., Xue, M. and Kong, F. (2014). Evaluating the performance of planetary
543 boundary layer and cloud microphysical parameterization schemes in convection-permitting
544 ensemble forecasts using synthetic GOES-13 satellite observations. Monthly Weather Review
545 142(1): 163-182.

546 Ćurić, M., Janc, D., Vučković, V. and Kovačević, N. (2009). The impact of the choice of the
547 entire drop size distribution function on Cumulonimbus characteristics. Meteorologische
548 Zeitschrift 18(2): 207-222.

549 Dai, Q. and Han, D. (2014). Exploration of discrepancy between radar and gauge rainfall
550 estimates driven by wind fields. Water Resources Research 50(11): 8571-8588.

551 Dai, Q., Bray, M., Zhuo, L., Islam, T., and Han, D. (2017). A scheme for raingauge network
552 design based on remotely-sensed rainfall measurements. Journal of Hydrometeorology 18: 363-
553 379.

554 Dai, Q., Yang, Q., Han, D., Rico - Ramirez, M. A., and Zhang, S. (2019). Adjustment of radar -
555 gauge rainfall discrepancy due to raindrop drift and evaporation using the Weather Research and
556 Forecasting model and dual-polarization radar. Water Resources Research 55: 9211-9233.

557 Davison, P., Hutchins, M., Anthony, S., Betson, M., Johnson, C. and Lord, E. (2005). The
558 relationship between potentially erosive storm energy and daily rainfall quantity in England and
559 Wales. *Science of the Total Environment* 344(1-3): 15-25.

560 De Roo, A., Wesseling, C. and Ritsema, C. (1996). LISEM: a single - event physically based
561 hydrological and soil erosion model for drainage basins. I: theory, input and output. *Hydrological
562 Processes* 10(8): 1107-1117.

563 Dee, D. P., Uppala, S., Simmons, A., Berrisford, P., Poli, P., Kobayashi, S., Andrae, U.,
564 Balmaseda, M., Balsamo, G. and Bauer, d. P. (2011). The ERA - Interim reanalysis:
565 Configuration and performance of the data assimilation system. *Quarterly Journal of the Royal
566 Meteorological Society* 137(656): 553-597.

567 Defra (2009). *Safeguarding our soils—A strategy for England*. Defra, UK.

568 Doelling, I. G., Joss, J. and Riedl, J. (1998). Systematic variations of Z–R-relationships from
569 drop size distributions measured in northern Germany during seven years. *Atmospheric Research*
570 47: 635-649.

571 Duck, R. W. (1996). Regional variations of fluvial sediment yield in eastern Scotland. *Erosion
572 and Sediment Yield: Global and Regional Perspectives* 236:157-161.

573 Dudhia, J. (1989). Numerical study of convection observed during the winter monsoon
574 experiment using a mesoscale two-dimensional model. *Journal of the Atmospheric Sciences*
575 46(20): 3077-3107.

576 EA (2004). *The state of soils in England and Wales*. Environment Agency, UK.

577 Ek, M., Mitchell, K., Lin, Y., Rogers, E., Grunmann, P., Koren, V., Gayno, G. and Tarpley, J.
578 (2003). Implementation of Noah land surface model advances in the National Centers for
579 Environmental Prediction operational mesoscale Eta model. *Journal of Geophysical Research:
580 Atmospheres* 108(22):8851.

581 Evans, R. (1990). Soils at risk of accelerated erosion in England and Wales. *Soil use and
582 Management* 6(3): 125-131.

583 Fornis, R. L., Vermeulen, H. R. and Nieuwenhuis, J. D. (2005). Kinetic energy–rainfall intensity
584 relationship for Central Cebu, Philippines for soil erosion studies. *Journal of Hydrology* 300(1-4):
585 20-32.

586 Gilmore, M. S., Straka, J. M. and Rasmussen, E. N. (2004). Precipitation uncertainty due to
587 variations in precipitation particle parameters within a simple microphysics scheme. *Monthly*
588 *Weather Review* 132(11): 2610-2627.

589 Hanel, M., Máca, P., Bašta, P., Vlnas, R. and Pech, P. (2016). The rainfall erosivity factor in the
590 Czech Republic and its uncertainty. *Hydrology and Earth System Sciences* 20(10): 4307-4322.

591 Hong, S.-Y., Lim, K.-S. S., Lee, Y.-H., Ha, J.-C., Kim, H.-W., Ham, S.-J. and Dudhia, J. (2010).
592 Evaluation of the WRF double-moment 6-class microphysics scheme for precipitating
593 convection. *Advances in Meteorology* 2010.

594 Hudson, N. (1963). Raindrop size distribution in high intensity storms. *Rhodesian Journal of*
595 *Agricultural Research* 1(1): 6-11.

596 Islam, T., Rico-Ramirez, M. A., Thurai, M. and Han, D. (2012). Characteristics of raindrop
597 spectra as normalized gamma distribution from a Joss–Waldvogel disdrometer. *Atmospheric*
598 *Research* 108: 57-73.

599 Janjić, Z. I. (1994). The step-mountain eta coordinate model: Further developments of the
600 convection, viscous sublayer, and turbulence closure schemes. *Monthly Weather Review* 122(5):
601 927-945.

602 Johnson, M., Jung, Y., Dawson, D. T. and Xue, M. (2016). Comparison of simulated
603 polarimetric signatures in idealized supercell storms using two-moment bulk microphysics
604 schemes in WRF. *Monthly Weather Review* 144(3): 971-996.

605 Jones, D. M. A. (1959). The shape of raindrops. *Journal of the Atmospheric Sciences* 16(1): 511-
606 515.

607 Jung, Y., Xue, M. and Zhang, G. (2010). Simulations of polarimetric radar signatures of a
608 supercell storm using a two-moment bulk microphysics scheme. *Journal of Applied Meteorology*
609 *and Climatology* 49(1): 146-163.

610 Kain, J. S. (2004). The Kain–Fritsch convective parameterization: an update. *Journal of Applied*
611 *Meteorology* 43(1): 170-181.

612 Kinnell, P. (1981). Rainfall intensity-kinetic energy relationships for soil loss prediction. *Soil*
613 *Science Society of America Journal* 45(1): 153-155.

614 Kinnell, P. and Risse, L. (1998). USLE-M: empirical modeling rainfall erosion through runoff
615 and sediment concentration. *Soil Science Society of America Journal* 62(6): 1667-1672.

616 Lim, K.-S. S. and Hong, S.-Y. (2010). Development of an effective double-moment cloud
617 microphysics scheme with prognostic cloud condensation nuclei (CCN) for weather and climate
618 models. *Monthly Weather Review* 138(5): 1587-1612.

619 Lim, Y. S., Kim, J. K., Kim, J. W., Park, B. I. and Kim, M. S. (2015). Analysis of the
620 relationship between the kinetic energy and intensity of rainfall in Daejeon, Korea. *Quaternary*
621 *International* 384: 107-117.

622 Marshall, J. S. and Palmer, W. M. K. (1948). The distribution of raindrops with size. *Journal of*
623 *Meteorology* 5(4): 165-166.

624 McIsaac, G. (1990). Apparent geographic and atmospheric influences on raindrop sizes and
625 rainfall kinetic energy. *Journal of Soil and Water Conservation* 45(6): 663-666.

626 Meshesha, D. T., Tsunekawa, A. and Haregeweyn, N. (2019). Influence of raindrop size on
627 rainfall intensity, kinetic energy, and erosivity in a sub-humid tropical area: a case study in the
628 northern highlands of Ethiopia. *Theoretical and Applied Climatology* 136(3-4): 1221-1231.

629 Meshesha, D. T., Tsunekawa, A., Tsubo, M., Haregeweyn, N. and Adgo, E. (2014). Drop size
630 distribution and kinetic energy load of rainfall events in the highlands of the Central Rift Valley,
631 Ethiopia. *Hydrological Sciences Journal* 59(12): 2203-2215.

632 Meshesha, D. T., Tsunekawa, A., Tsubo, M., Haregeweyn, N. and Tegegne, F. (2016).
633 Evaluation of kinetic energy and erosivity potential of simulated rainfall using Laser
634 Precipitation Monitor. *Catena* 137: 237-243.

635 Mikoš, M., Jošt, D. and Petkovšek, G. (2006). Rainfall and runoff erosivity in the alpine climate
636 of north Slovenia: a comparison of different estimation methods. *Hydrological sciences journal*
637 51(1): 115-126.

638 Mlawer, E. J., Taubman, S. J., Brown, P. D., Iacono, M. J. and Clough, S. A. (1997). Radiative
639 transfer for inhomogeneous atmospheres: RRTM, a validated correlated - k model for the
640 longwave. *Journal of Geophysical Research: Atmospheres* 102(14): 16663-16682.

641 MO (2012). Met Office Integrated Data Archive System (MIDAS) land and marine surface
642 stations data (1853 - current).

643 Montopoli, M., Marzano, F. S. and Vulpiani, G. (2008). Analysis and synthesis of raindrop size
644 distribution time series from disdrometer data. *IEEE Transactions on Geoscience and Remote
645 Sensing* 46(2): 466-478.

646 Morgan, R. (1985). Assessment of soil erosion risk in England and Wales. *Soil use and
647 Management* 1(4): 127-131.

648 Morrison, H., Milbrandt, J. A., Bryan, G. H., Ikeda, K., Tessorf, S. A. and Thompson, G.
649 (2015). Parameterization of cloud microphysics based on the prediction of bulk ice particle
650 properties. Part II: Case study comparisons with observations and other schemes. *Journal of the
651 Atmospheric Sciences* 72(1): 312-339.

652 Morrison, H., Thompson, G. and Tatarskii, V. (2009). Impact of cloud microphysics on the
653 development of trailing stratiform precipitation in a simulated squall line: Comparison of one-
654 and two-moment schemes. *Monthly weather review* 137(3): 991-1007.

655 Nyssen, J., Vandenreyken, H., Poesen, J., Moeyersons, J., Deckers, J., Haile, M., Salles, C. and
656 Govers, G. (2005). Rainfall erosivity and variability in the Northern Ethiopian Highlands.
657 *Journal of Hydrology* 311(1-4): 172-187.

658 O'Neill, D. (2007). The total external environmental costs and benefits of agriculture in the UK.
659 Environment Agency, UK.

660 Panagos, P., Ballabio, C., Borrelli, P., Meusburger, K., Klik, A., Rousseva, S., Tadić, M. P.,
661 Michaelides, S., Hrabalová M. and Olsen, P. (2015a). Rainfall erosivity in Europe. *Science of
662 the Total Environment* 511: 801-814.

663 Panagos, P., Borrelli, P., Poesen, J., Ballabio, C., Lugato, E., Meusburger, K., Montanarella, L.
664 and Alewell, C. (2015b). The new assessment of soil loss by water erosion in Europe.
665 *Environmental Science & Policy* 54: 438-447.

666 Park, S., Mitchell, J. and Bubenzer, G. (1982). Splash erosion modeling: physical analysis.
667 Transactions of the ASAE 25:357-361.

668 Petan, S., Rusjan, S., Vidmar, A. and Mikoš, M. (2010). The rainfall kinetic energy–intensity
669 relationship for rainfall erosivity estimation in the mediterranean part of Slovenia. Journal of
670 Hydrology 391(3-4): 314-321.

671 [Pickering, B. S., Neely III, R. R., & Harrison, D. \(2019\). The Disdrometer Verification Network](#)
672 [\(DiVeN\): a UK network of laser precipitation instruments. Atmospheric Measurement](#)
673 [Techniques 12: 5845-5861.](#)

674 Prigent, C. (2010). Precipitation retrieval from space: An overview. Comptes Rendus Geoscience
675 342(4-5): 380-389.

676 Renard, K. G., Foster, G. R., Weesies, G., McCool, D. and Yoder, D. (1997). Predicting soil
677 erosion by water: a guide to conservation planning with the Revised Universal Soil Loss
678 Equation (RUSLE), United States Department of Agriculture Washington, DC.

679 Rosewell, C. J. (1986). Rainfall kinetic energy in eastern Australia. Journal of Climate and
680 Applied Meteorology 25(11): 1695-1701.

681 Sanchez-Moreno, J. F., Mannaerts, C. M., Jetten, V. and Löffler-Mang, M. (2012). Rainfall
682 kinetic energy–intensity and rainfall momentum–intensity relationships for Cape Verde. Journal
683 of Hydrology 454: 131-140.

684 Sempere - Torres, D., Porrà, J. M. and Creutin, J. D. (1998). Experimental evidence of a general
685 description for raindrop size distribution properties. Journal of Geophysical Research:
686 Atmospheres 103(2): 1785-1797.

687 Song, Y., Han, D. and Rico-Ramirez, M. A. (2017). High temporal resolution rainfall rate
688 estimation from rain gauge measurements. Journal of Hydroinformatics 19(6): 930-941.

689 Thompson, G. and Eidhammer, T. (2014). A study of aerosol impacts on clouds and precipitation
690 development in a large winter cyclone. Journal of the Atmospheric Sciences 71(10): 3636-3658.

691 Uplinger, W. (1981). A new formula for raindrop terminal velocity. Conference on Radar
692 Meteorology, 20 th, Boston, MA.

693 Van Dijk, A., Bruijnzeel, L. and Rosewell, C. (2002). Rainfall intensity–kinetic energy
694 relationships: a critical literature appraisal. *Journal of Hydrology* 261(1-4): 1-23.

695 Wang, L., Shi, Z., Wang, J., Fang, N., Wu, G. and Zhang, H. (2014). Rainfall kinetic energy
696 controlling erosion processes and sediment sorting on steep hillslopes: a case study of clay loam
697 soil from the Loess Plateau, China. *Journal of Hydrology* 512: 168-176.

698 Weiss, L. L. (1964). Ratio of true to fixed-interval maximum rainfall. *Journal of the Hydraulics*
699 *Division* 90(1): 77-82.

700 Williams, R. and Sheridan, J. (1991). Effect of rainfall measurement time and depth resolution
701 on EI calculation. *Transactions of the ASAE* 34(2): 402-0406.

702 Wischmeier, W. H. and Smith, D. D. (1958). Rainfall energy and its relationship to soil loss. *Eos,*
703 *Transactions American Geophysical Union* 39(2): 285-291.

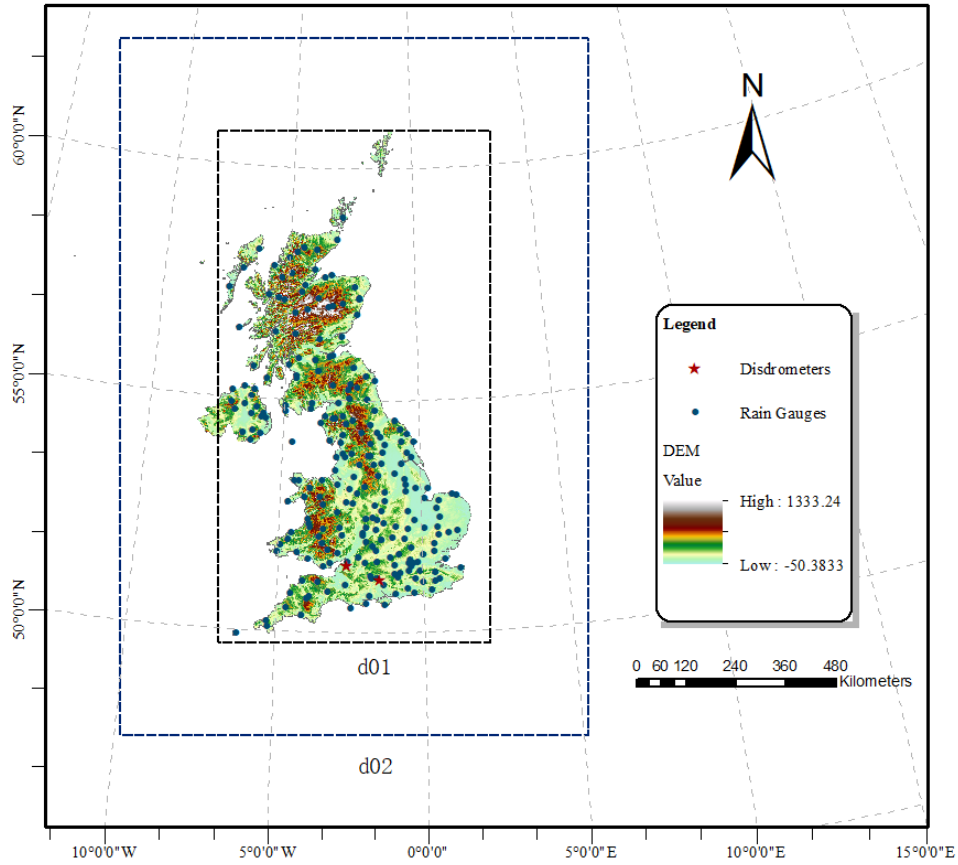
704 Wischmeier, W. H. and Smith, D. D. (1978). Predicting rainfall erosion losses-a guide to
705 conservation planning. Department of Agriculture, Science and Education Administration, US.

706 Xie, Y., Yin, S., Liu, B., Nearing, M. A. and Zhao, Y. (2016). Models for estimating daily
707 rainfall erosivity in China. *Journal of Hydrology* 535: 547-558.

708 Yang, Q., Dai, Q., Han, D., Chen, Y., and Zhang, S. (2019). Sensitivity analysis of raindrop size
709 distribution parameterizations in weather research and forecasting rainfall simulation.
710 *Atmospheric Research* 228:1-13.

711

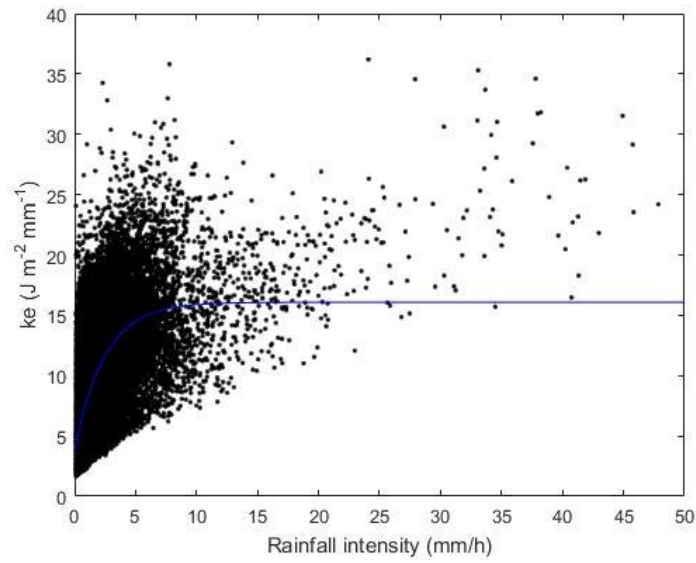
712



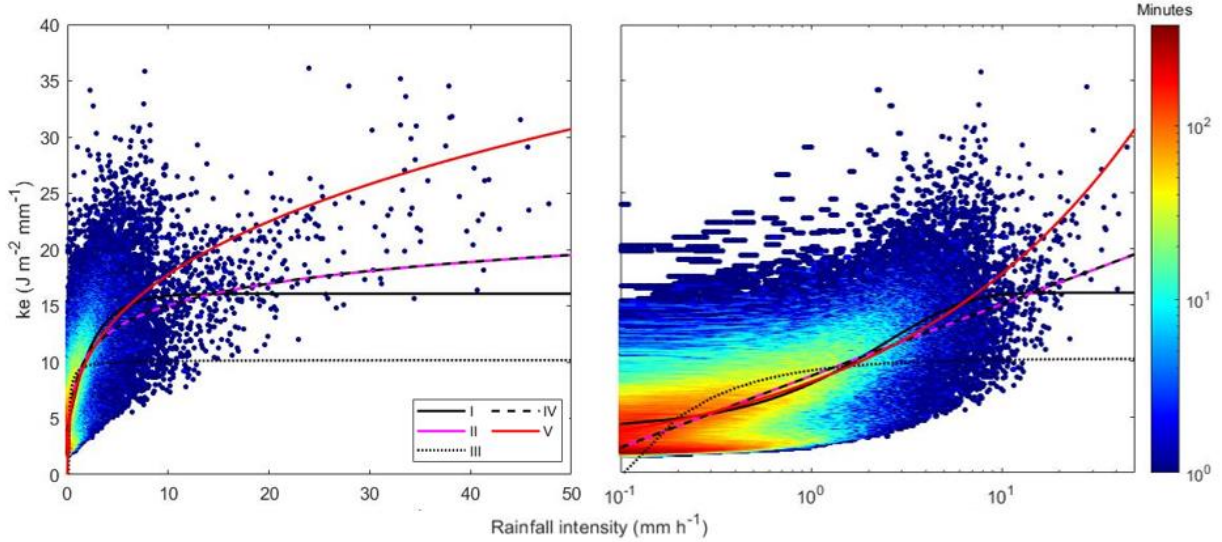
713

714 **Figure 1.** Location of rain gauges, Joss–Waldvogel disdrometer (JWD) at Chilbolton
 715 Observatory, OTT Parsivel² disdrometer (OPD) at Bristol Observatory and configurations of
 716 domain setups in the WRF model.

717



718

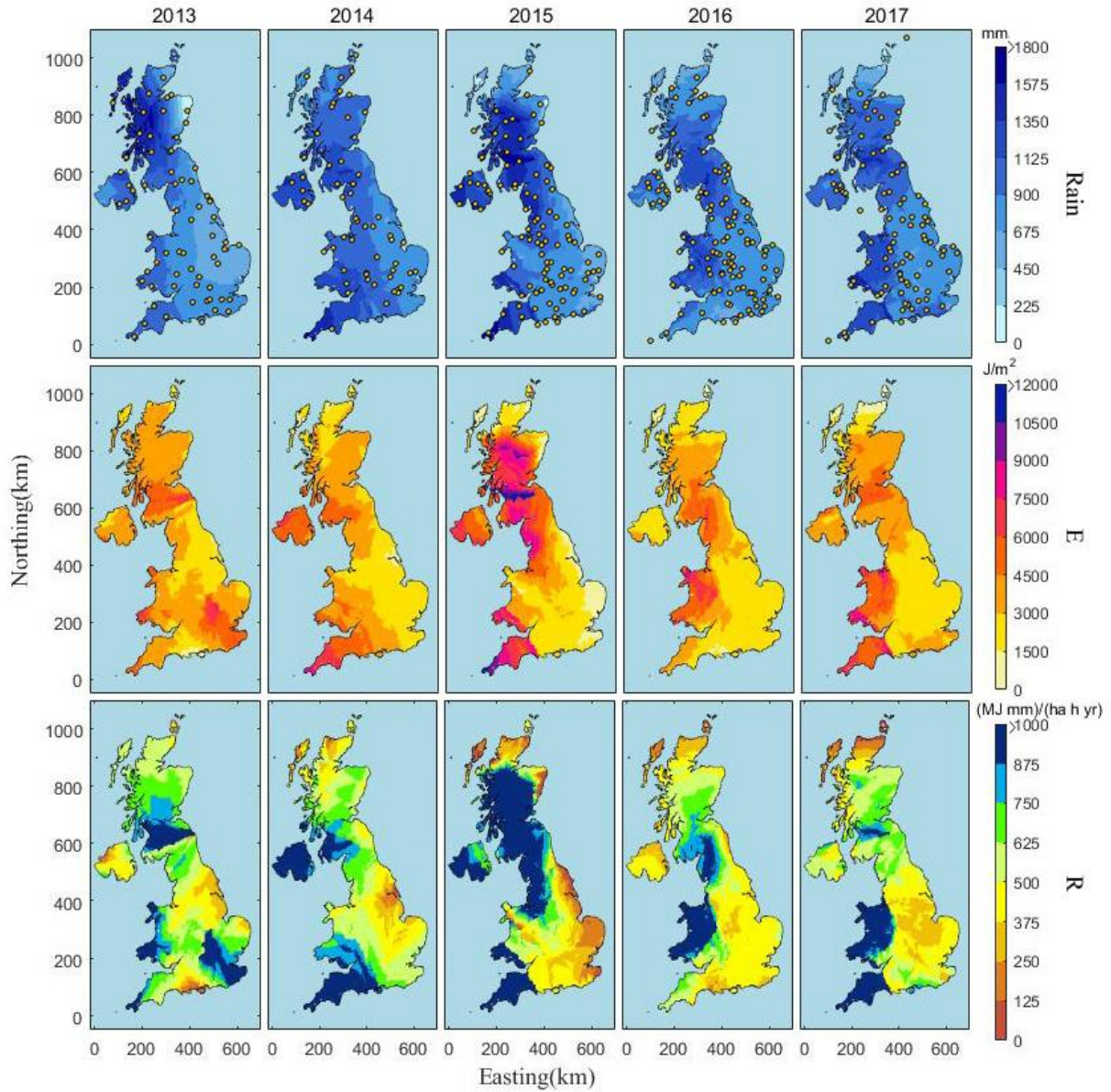


719

720

721 **Figure 2.** Minutes number per intensity class (x-axis) and ke class (y-axis) with five fitted $ke-I$
 722 curves at Chilbolton station (2004–2013), plotted on linear (left) and logarithmic (right) intensity
 723 scales. The fitted relationship of $ke-I$ based on exponential regression (2004–2013).

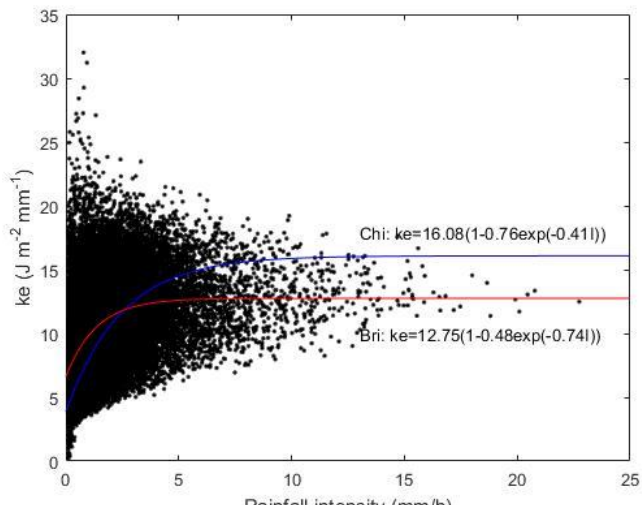
724



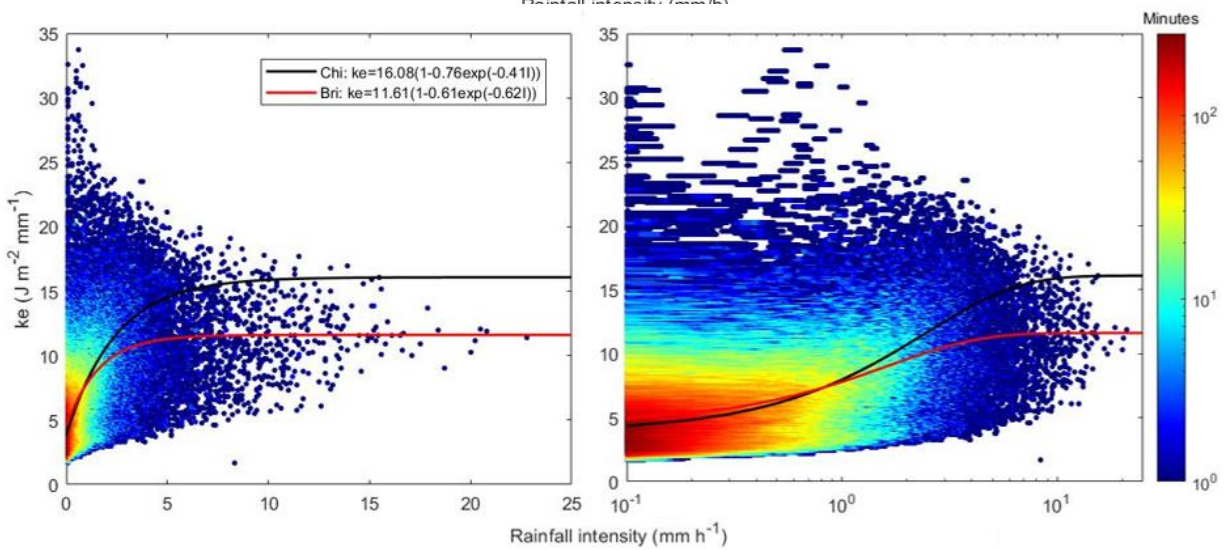
725

726 **Figure 3.** Gauge-based interpolation maps of annual rainfall amount (*Rain*), rainfall kinetic
 727 energy (*E*) and rainfall erosivity (*R*) in 2013–2017.

728



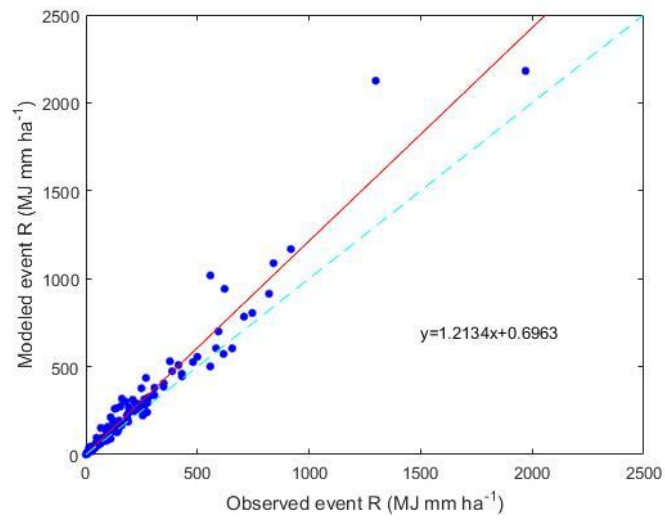
729



730

731 **Figure 4.** Minutes number per intensity class (x-axis) and ke class (y-axis) with fitted $ke-I$
 732 curves at Bristol station (2015–2018), plotted on linear (left) and logarithmic (right) intensity
 733 scales. Relationship of $ke-I$ at Bristol station.

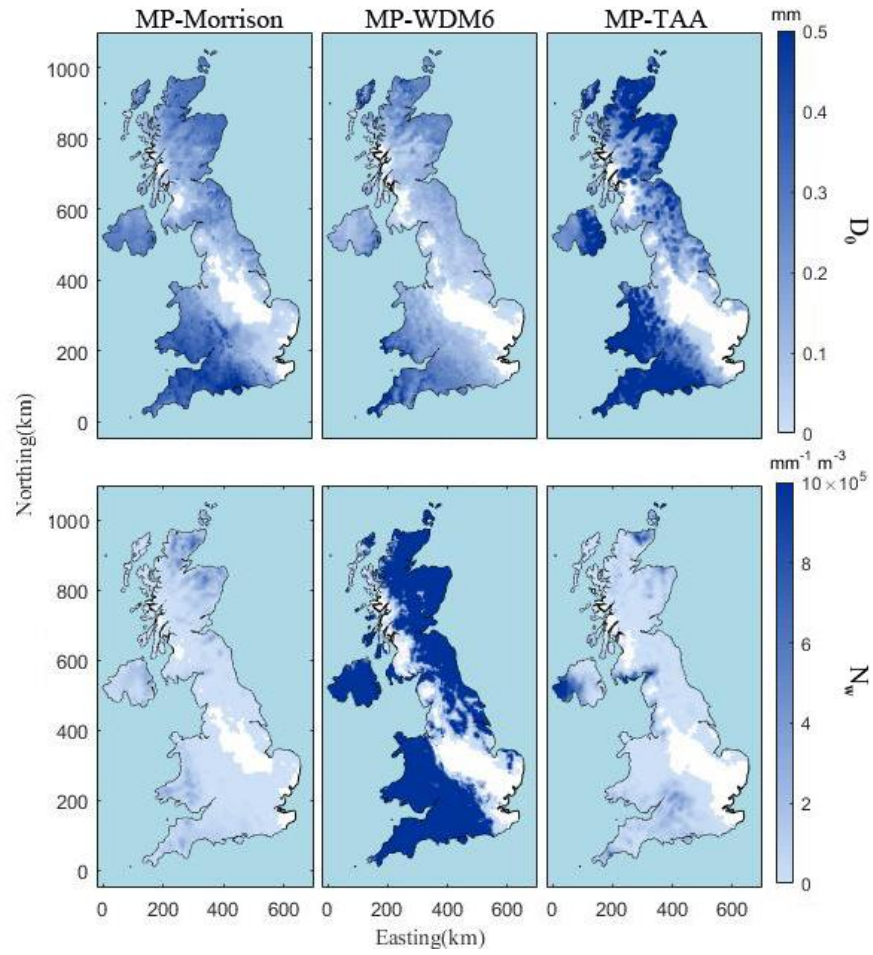
734



735

736 **Figure 5.** Comparison of observed and modeled event rainfall erosivity at Bristol Station,
737 covering the period of 2016–2019.

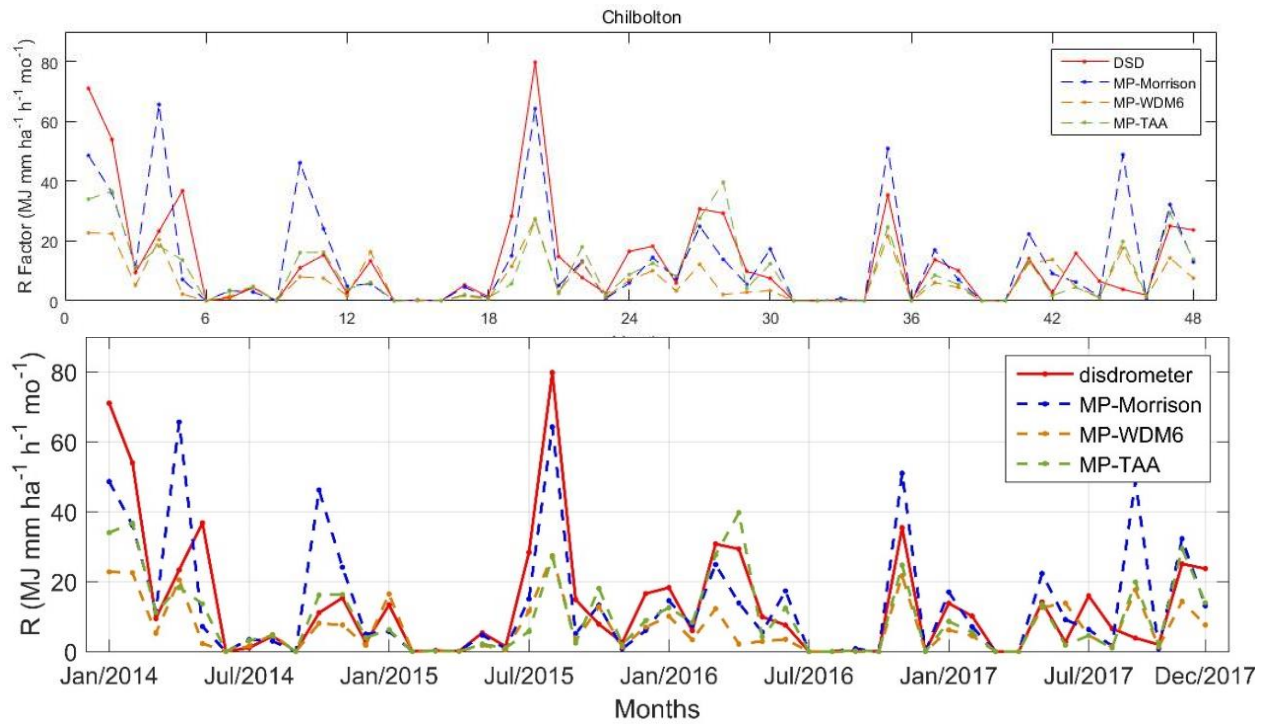
738



739

740 **Figure 6.** Map of average WRF DSD D_0 and N_w (January 10, 2013).

741

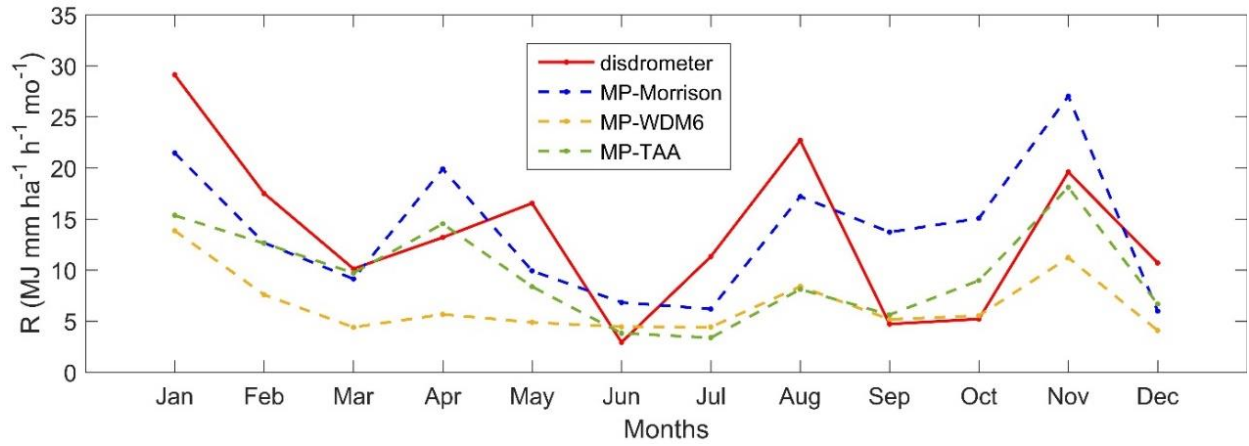


742

743

744 **Figure 7.** Comparison of disdrometer- and WRF-derived monthly rainfall erosivity estimations
 745 at Chilbolton station [\(2014–2017\)](#).

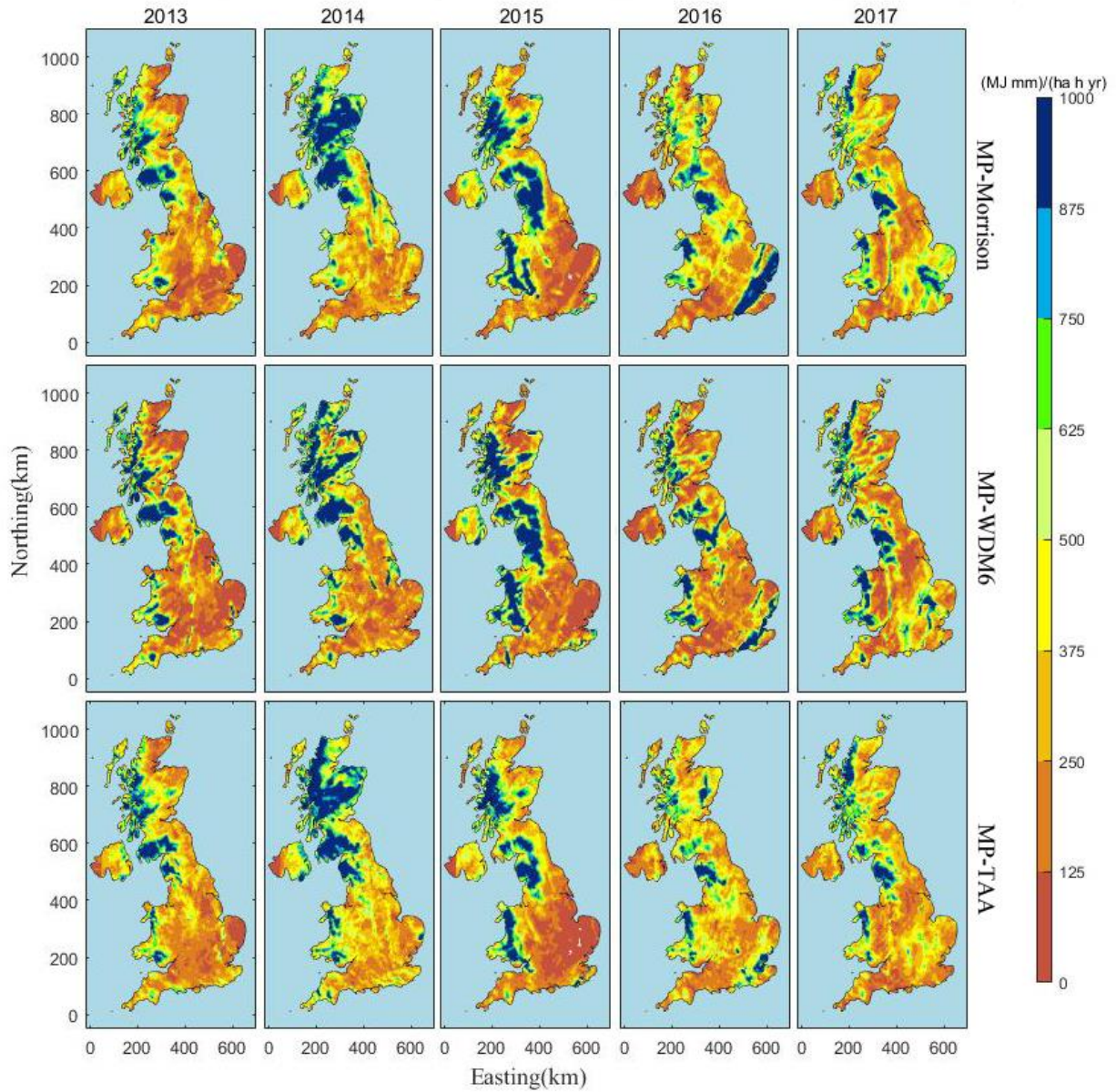
746



747

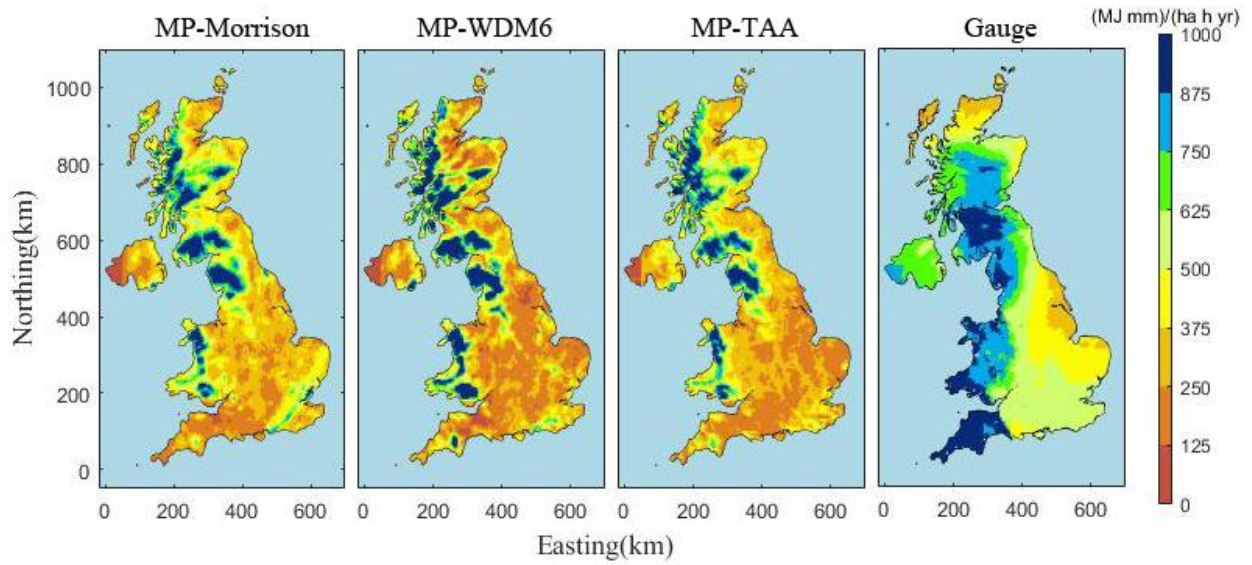
748 **Figure 8.** Comparison of disdrometer- and WRF-derived average monthly rainfall erosivity
 749 estimations at Chilbolton station (2014–2017).

750



751
752
753

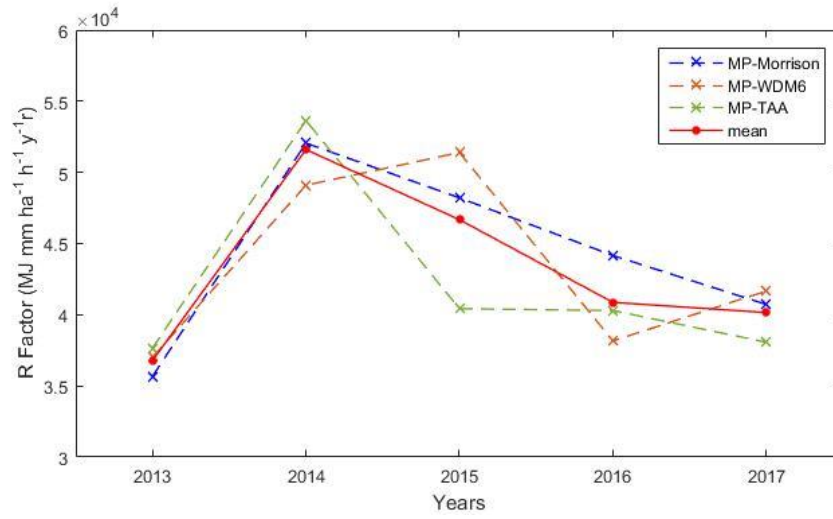
Figure 89. WRF-derived R_w -annual rainfall erosivity maps of the whole UK for different years.



754

755 **Figure 109.** The 5-year (2013–2017) average R-annual rainfall erosivity maps based on WRF
 756 grids and rain gauge interpolation.

757



758

759 **Figure 1011.** The WRF-derived average annual rainfall erosivity R_w of all the WRF grids
 760 covering the whole UK (2013–2017).

761

762

Table 1. Relationship of $ke-I$ at Chilbolton Station (2004–2013).

ID	Equation	Calibration R²	Validation R²
I	$ke = 16.08(1 - 0.76e^{-0.41I})$	0.50	0.45
II	$ke = 8.65 + 6.39 \lg(I)$	0.48	0.43
III	$ke = 10.19 - 1.05/I$	0.29	0.25
IV	$ke = 8.65 + 2.78 \ln(I)$	0.48	0.43
V	$ke = 8.12I^{0.34}$	0.50	0.45

763

764

765 **Table 2.** The configurations of WRF model for two nested domains.

Domain	Domain size (km)	Grid Spacing (km)	Grid size	Downscaling ratio
d01	1,125 × 1,675	25	45 × 67	-
d02	655 × 1,230	5	131 × 246	1:5

766

767

768 **Table 3.** Indicators comparison between disdrometer-derived rainfall erosivity R_D and three
 769 types of WRF-derived rainfall erosivity R_w -at Chilbolton station on monthly scale (2014-2017).

Indicators	MP-Morrison	MP-WDM6	MP-TAA
Pearson	0.71	0.77	0.79
MAE	8.05	8.42	6.51
R ²	0.42	0.31	0.54

770